UNIVERSITÀ DEGLI STUDI DI PADOVA

Dipartimento di Fisica e Astronomia "Galileo Galilei"

Master Degree in Physics

Final Dissertation

Optical control of droplet motion on Fe-doped lithium niobate crystals via photovoltaic effect

Thesis supervisor

Prof. Giampaolo Mistura

Thesis co-supervisor

Dr. Annamaria Zaltron

Candidate

Sofia Saoncella

Academic Year 2018/2019

Abstract

This thesis presents the innovative study on the local modification of surface wettability actuated by light by exploiting the photovoltaic properties of a photorefractive material, a lithium niobate crystal doped with iron. The project advances the first step towards the improvement of the already available electrowetting technology which uses electric voltages to manipulate aqueous droplets over metallic electrodes. The novel optowetting technique is aimed to get rid of fixed electrodes and hence to provide multi-purpose devices. Lithium niobate samples were properly selected and characterized and a search for the most suitable dielectric film was conducted in order to optimize the optowetting performances of the system. The wettability of the functionalized surfaces was evaluated by means of the contact angle of 1 μL water droplets and, using a systematic measurement protocol, the dynamics of the phenomenon was investigated. The results obtained shows that the virtual electrodes induced on the crystal surface by a laser source have a temporal duration of several hours in the case of specific compositional properties of the substrate coupled with a thin dielectric layer of PDMS. In addiction, the characteristic time of the optowetting effect can be tuned by regulating the intensity of excitation light, the thickness of the dielectric layer and by varying the reduction degree of iron of the lithium niobate crystal. A final experiment demonstrated the feasibility of such a device. A virtual electrode was traced as an optical path using a 532 nm laser on the treated surface sample and it was observed that the motion of a water droplet driven by gravity on the sample was modified as it ran into the optical path.

Contents

List of Figures

Introduction

Since the advent of microfluidics, approximately two decades ago, there has been a steady increase in the interest and development of tools to control fluid flow at the microscale. Microfluidic technology's success is due to the fact that the volume of reagents can be significantly reduced from milliliters and microliters to nanoliters and femtoliters with a consequent reduction of the time needed to perform typical laboratory operations.
Among the several techniques which have been developed to control reduced quantities of fluids, electrowetting (EW) has emerged as a powerful tool to electrically manipulate tiny individual droplets in a controlled manner [20]. EW and, in particular, electrowetting on dielectric (EWOD) are methods which allow to control the wettability of liquids on solid surfaces using electric potential. While EW consists in controlling the wettability of a certain electrolyte on a metal electrode by varying electric energy across the electrical double layer, EWOD applies to virtually any aqueous liquid by varying electric energy across the thin dielectric film between the liquid and conducting substrate. These driving mechanisms have many advantages. By electrically changing the wettability of each of the electrode patterns on a surface, a liquid on these electrodes can be shaped and driven along the active electrodes, making microfluidics extremely simple both for device fabrication and operation. It is also worth noting that, driven by surface tension, the mechanism becomes more effective as the size of the device becomes smaller. However, electrowetting technology relies on the implementation into the microfluidic chip of metallic electrodes, which are fixed structures with little possibility to adapt to new manipulation purposes without a complete change of the device.
In this case, a solution is provided by optofluidics, which refers not only to the manipulation of light by liquids, as droplet lens or liquid waveguides [26], but above all to the possibility of actuating fluids by means of optically induced forces [11, 21, 4]. A promising material for realizing optofluidic devices is lithium niobate ($LiNbO_3$), a well-known material in photonics which has recently demonstrated to be a viable candidate also for combining its excellent optical properties with the potentialities offered by microfluidics [8, 10, 7].

In this thesis, the novel concept of *optowetting* is exploited towards the realization and the characterization of a dedicated device. The focus of the project is the investigation of lithium niobate as active substrate for varying the wetting properties of the crystal surface by means of virtual electrodes, which are induced by light at the surface of the material via the photovoltaic effect. The photovoltaic effect consists in the creation of an electric current inside a material when it is exposed to light of proper wavelength. The photo-excited charge carriers move inside the material mainly along a preferred crystallographic direction till a dark region is reached and they could not be further excited by light; in this way, the charge carriers accumulate at the borders of the illuminated area and the resulting charge separations give rise to strong photovoltaic electric fields. It is well known in literature [24] that the phenomenon is significantly enhanced when the material is doped with iron (Fe:$LiNbO_3$): Fe ions are incorporated into the lithium niobate matrix with two possible valence states, Fe^{2+} and Fe^{3+}, which act as donors and acceptors of charge carriers, respectively. In this way it is possible to obtain photovoltaic fields up to 10^6 V/m, which can be exploited for the actuation of particles and liquids. As a matter of fact, the time constant typical of this phenomenon is directly affected by the Fe reduction degree (i.e. the ratio Fe^{2+}/Fe^{2+}), therefore, this parameter is investigated to optimize the light-driven change of substrate wettability.

It is worth mentioning that one of the main advantages of $LiNbO_3$-based electrowetting is represented by its high reconfigurability. Indeed, the charge accumulations and electric fields created by light at the surface of this material can be efficiently erased with proper uniform illumination, so that the geometry of the virtual electrodes can be rapidly erased and adapted to the desired goal of the device.

A consistent part of the work was dedicated to the study of different dielectric films: the chemical depositions of silicon-based chemicals OTS and FTS and a coating of polydimethylsiloxane (PDMS) were realized on the surface of $LiNbO_3$ samples to increase their hydrophobicity; moreover, the thickness of the PDMS films was varied, since this parameter was expected to significantly affect the final manipulation performance of the material.
On the most performant lithium niobate crystals, local changes of the surface wettability were induced by light and their capability in controlling droplets shape was systematically characterized through the measurement of the contact angles of the droplets.
As a final demonstration of the applicability of the optowetting mechanism, the study of water drops sliding down an optically heterogeneous surface was done: an optical path was traced across the functionalized crystal and a deviation of the droplet motion in correspondence of the hydrophilic stripe was recorded.

The thesis is structured as follows:

- **Chapter 1**: the theoretical basis of surface wetting are recalled and the general characteristics and methods related to the electrowetting and electrowetting on dielectric techniques are described;
- **Chapter 2**: the characteristics of lithium niobate are described in a general way: the chemical composition, the crystalline structure and in particular the physical and optical properties that are of interest for this thesis work;
- **Chapter 3**: a detailed description of the procedures used to produce the samples, the optical absorption method to characterize their compositional properties and the realization of the hydrophobic coatings is given;
- **Chapter 4**: the experimental apparatus, together with the measurement procedures and the instruments used for the analysis are described;
- **Chapter 5**: the experimental results are presented.

Chapter 1

Fundamental Concepts of Wetting

In this chapter the basic concepts necessary to understand the themes discussed in this thesis will be explained. The wettability describes the way in which the liquid spreads on a solid substrate and by means of the electrowetting method, here described, it can be modified; the result is a fine tuning of the shape of a liquid droplet deposited on a metallic electrode.

1.1 Surface Tension

A density discontinuity exists whenever two immiscible fluids are in contact, for example at the interface between water and air. The interface in this case is found to behave as it were under tension like the stretched membrane of a balloon or a soap bubble. This is why drops in air or gas bubbles in water tends to have a spherical shape.
The origin of such a tension in an interface is due to the intermolecular attractive forces between the two phases in contact. Considering a water drop surrounded by air, each liquid molecule is subject to cohesive interactions (e.g. Van der Waals type, hydrogen bonds, etc.) exerted by the surrounding molecules. A molecule in the bulk is isotropically surrounded by neighbours yielding a total attractive energy U. Conversely, a molecule at the interface interacts anisotropically with almost half neighbours and it is subject to a total energy $U/2$, as shown in Figure 1.1. The *surface tension* γ is a direct measure of this energy shortfall per unit surface area. If a is the molecule's size and a^2 is its exposed area, the surface tension is of order $\gamma \cong U/(2a^2)$ [5]. Therefore the drop will tend to minimize its surface area, hence it will converge in the state of minimum free energy. In order to increase the drop surface it is necessary to do a work on the interface. The work required is proportional to the number of molecules that must be brought up to the surface, i.e., to the unit of surface dA; hence one can write:

$$dW = \gamma \cdot dA \tag{1.1}$$

where dW indicates the external work. This quantity is indeed a surface energy density which has the unit $\mathrm{J/m^2}$.

An important consequence of surface tension is that it gives rise to a pressure jump across the interface whenever it is curved. In particular, Laplace's law shows that across a curved interface in mechanical equilibrium there is a pressure difference Δp proportional to γ:

$$\Delta p = \gamma \left(\frac{1}{R_1} + \frac{1}{R_2} \right) \tag{1.2}$$

where R_1 and R_2 are the two main curvature radii of the surface.
An important parameter that concerns the capillary phenomena is the *Bond number* which measures the strength of gravity with respect to surface tension, defined as

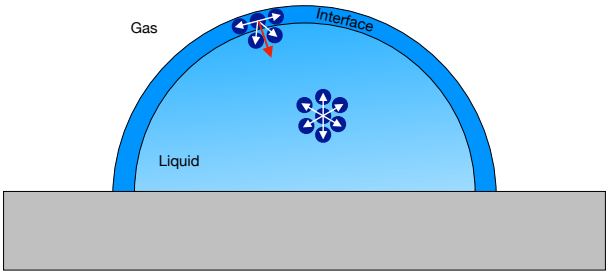

Figure 1.1: Microscopic origin of surface tension: molecules at the liquid/gas interface interact with less neighbours than molecules in the bulk.

$$B_o = \frac{\rho g L^2}{\gamma} \tag{1.3}$$

where ρ is the viscosity, g is gravity acceleration and L is the characteristic length of the system. In this work, as in most applications of interest, systems of single water droplets with a typical size of the order of 1 mm will be discussed. Under these conditions the Bond number is smaller than unity, therefore gravity contribution can be neglected in the following considerations.

1.2 Wetting of Surfaces

The notion of wettability, described for the first time by Young two centuries ago, describes how a liquid drop distributes when deposited on a solid surface. Such a system is characterized by the presence of three interfaces: liquid-solid, air-solid and liquid-air, as in Figure 1.2. The line where the three phases are present at the same time is defined *contact line* and it delimits the area wetted by the liquid. Wetting of a solid surface by liquid can be quantitatively described from the profile of a liquid droplet, more specifically from the tangential angle at liquid–solid–air interface. This angle of contact is defined as the Young's angle or static contact angle θ_Y. It is the result of a mechanical equilibrium among the three surface tensions, the liquid surface tension γ_{LV}, the solid surface tension γ_{SV}, and the liquid–solid interfacial tension γ_{SL} which is expressed with the Young's equation [19]:

$$\gamma_{SV} = \gamma_{LV} \cos\theta_Y + \gamma_{SL} \tag{1.4}$$

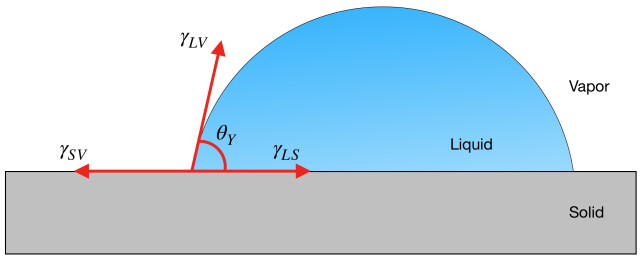

Figure 1.2: Liquid drop on a solid surface with the surface tensions of the three interfaces.

In contrast to surface tensions, the contact angle can be directly and quite simply measured by optical imaging. For this reason the wettability of a surface is defined in term of contact angle for a water drop:

- if $\theta_Y < 90°$ the surface is *hydrophilic*;
- if $90° < \theta_Y < 150°$ the surface is *hydrophobic*;

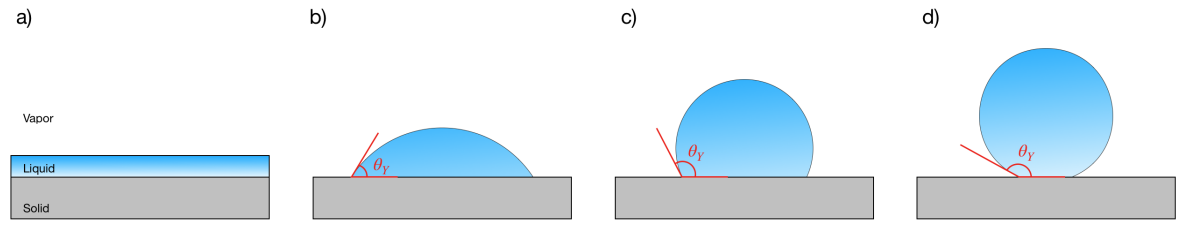

Figure 1.3: Wetting regimes: a) total wetting, b) hydrophilic surface, c) hydrophobic surface, d) superhydrophobic surface.

- if $\theta_Y > 150°$ the surface is *superhydrophobic*.

The *total wetting* regime is the case in which water completely spreads on the substrate forming a thin film and corresponds to the condition $\gamma_{LV} \leq \gamma_{SV} - \gamma_{SL}$.
In general, the term *lyophobic* (*lyophilic*) is used for liquids different from water, instead of hydrophobic (hydrophilic).

1.3 Electrowetting

In many microfluidic applications surface wetting is a crucial concept for fluids manipulations and in particular in the field of droplet-based microfluidics, in which actions like sorting, merging and mixing of droplets are essential to realize chemical or biomedical analysis in a controlled manner. For this reason several studies have been carried out in order to control the interfacial energy of surfaces and therefore to actively control the shape and the motion of liquid droplets. One of the most successful techniques aimed to this purpose is electrowetting which allows several tens of degree of switchability, high switchability speed, long term reliability and compatibility with variable environments.

1.3.1 Basics of electrowetting

Electrowetting (EW) arises from the studies carried out by Lippmann in 1875 on electrocapillarity and developed in 1990s by Berge [3], but the most relevant technological achievements have been reached in the past five years by a growing community of researchers in the field.
The technique is based on the application of a potential difference between two metallic electrodes which are in contact with a polar liquid drop. Switching on the voltage, a local concentration of charges arises in the metallic surface giving place to the so-called *double charge layer* at the solid-liquid interface [20]. A problem in this configuration was the electrolytic decomposition of water upon applying voltages beyond a few hundred millivolts. It was Berge who introduced the concept of *electrowetting on dielectric* (EWOD) using a thin insulating layer to separate the conductive liquid from the metallic electrode in order to eliminate the problem of electrolysis. In this configuration (see Figure 1.4) the uncompensated polarization charge in the dielectric layer interact with the dipole molecules in the liquid, thus redistributing them in the solid surface. Fundamentally, the wettability can be assumed as a local change at the solid-liquid interface due to the presence of the electric force.

The system can be described as two capacitors in series: the solid-insulator interface and the dielectric layer. The former has a capacitance $c_H = \varepsilon_0\varepsilon_1/d_H$ where ε_1 is the dielectric constant of the liquid and d_H is the thickness of the charges double layer of the order of few nanometers; the latter has a capacitance $c_d = \varepsilon_0\varepsilon_d/d$ indicating with ε_d the dielectric constant of the dielectric and d its thickness. Since $d_H \ll d$, the total capacitance per unit area is $c \approx c_d$. It can be demonstrated that the voltage drop occurs within the dielectric layer and the effective interfacial tension is

$$\gamma_{SL}^{eff} = \gamma_{SL} - \frac{\varepsilon_0\varepsilon_d}{2d}V^2 \tag{1.5}$$

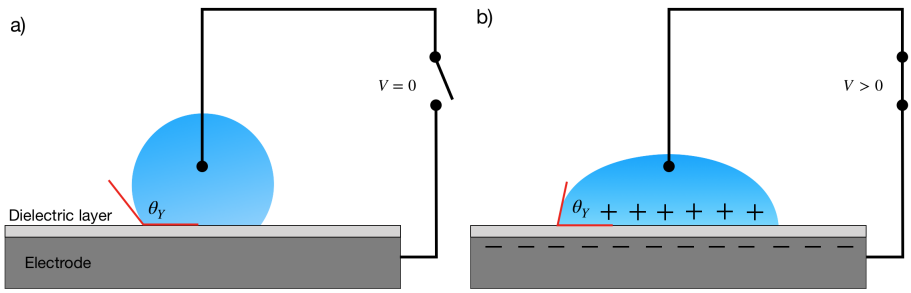

Figure 1.4: Schematic electrowetting setup. a) Partially wetting liquid droplet at zero voltage and b) at high voltage.

where V is the applied potential difference. Substituting this expression in Equation 1.4 the basic equation for EWOD is obtained:

$$\cos\theta = \cos\theta_Y + \frac{\varepsilon_0\varepsilon_d}{2d\gamma_{LV}}V^2 \tag{1.6}$$

However, this relation holds only at low voltages. In fact, beyond a certain system-dependent threshold value, the contact angle has been found to become independent on the applied voltage. In particular, no voltage-induced transition from partial to complete wetting has ever been observed. This phenomenon is called contact angle saturation. A number of physical explanations have been reported in order to explain this observation [20] but their diversity indicates that the contact angle saturation is a question still not well understood. Most probably, few competing processes occur at the same time and it seems to be clear that diverging electric fields at the contact line can induce several non-linear effects, each of which may independently cause saturation.

1.3.2 Materials properties for EWOD

In classical electrowetting theory, the liquid is treated as a perfect conductor. For aqueous salt solutions this corresponds to the limit of either high salt concentration or low frequency. As a matter of fact, in an aqueous solution the more ions are present, the more polarisable it is and, in the case of small variations of the applied AC voltage, the contact angle and droplet shape can follow adiabatically the temporary equilibrium values. For frequencies lower than 1 kHz even demineralized water displays significant electrowetting response [16]. Often EW experiments are performed with salt concentrations of the order of 0.01-1 mol/L but many authors report no significant influence due to the type or the concentration of the salt. This fluid manipulation technique can be exploited also with aqueous solutions containing biomolecules such as DNA or proteins and has even been demonstrated for physiological fluids [23]. Electrowetting is thus a rather robust phenomenon that weakly depends on the liquid properties. In contrast, the dielectric and geometrical properties of the insulating layers are much more critical.
A common requirement to enhance the efficiency of the method is to minimize the voltage required for the contact angle reduction. At the same time, the material used should be chemically inert and stable in order to ensure reproducibility and a long lifetime of the device. From Equation 1.6 two criteria to be met by the material can be derived: first, the contact angle at zero voltage should be as large as possible in order to achieve a large tuning range and, second, the dielectric layer should be as thin as possible. The first condition can be satisfied either using a chemically hydrophobic insulator, such as many polymer materials, or by covering hydrophilics insulators with a hydropobic coating. Commonly used coatings are silica-based coatings or fluorinated silanes or, more frequently, thin layers of amorphous fluoropolymer (Teflon) deposited by spin coating or dip coating.

With this work a novel technique for actuating EWOD is proposed by exploiting the physical properties of a photorefractive material to be used as a substrate: a lithium niobate crystal. A more accurate description of lithium niobate will be reported in the following chapter and the explanation of the innovative electrowetting application will be introduced in section 2.5.

Chapter 2

Lithium Niobate

In this chapter the main characteristics and the physical properties of lithium niobate crystals will be presented. The most relevant property of the material for this thesis work, the photovoltaic effect, is treated with more detail and in the final paragraph the new application of this material, which represents the aim of this thesis work, is presented and motivated.

2.1 Chemical Composition

Lithium niobate ($LiNbO_3$) is a synthetic material originating from the Li_2O–Nb_2O_5 system. Colourless, insoluble in water and in organic solvents, it has excellent chemical stability. As one can see from the phase diagram in Figure 2.1 there is a wide range of solubility of the two oxides at high temperatures, whose solid-liquid curve shows a maximum at 48.38% of Li_2O. Crystals with this composition are called *congruent* and have a Li-deficient structure compared to stoichiometric crystals for which instead the percentages of Li_2O and Nb_2O_5 are equal to 50%.

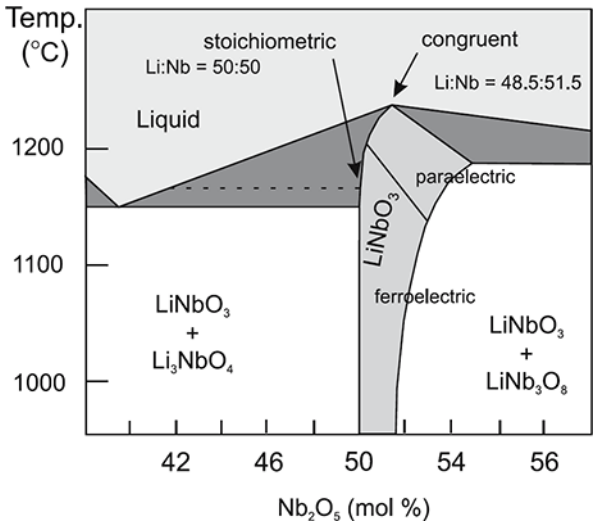

Figure 2.1: Phase diagram of the Li_2O–Nb_2O_5 system near the congruent and stoichiometric composition of $LiNbO_3$.

For the congruent lithium niobate, the melted and the solid crystals have the same composition, which is advantageous because it allows to obtain the best possible uniformity in the product. This is important because many properties depend on the ratio between the concentrations of Li and Nb, such as phase transition temperature, phase-matching temperature and position of the UV absorption edge [24]. As a result, due to the high sensitivity to compositional changes and the high stability achieved during the growth process, most commercial products are available in congruent composition.

Lithium niobate has numerous physical properties: it is pyroelectric, piezoelectric and has remarkable non-linear optical properties which make it a well-known material in the field of photonics and integrated optics.

2.2 Crystal Structure

To describe the structure of the crystal in the trigonal system, the definition of the crystallographic axes is not unambiguous and three different cells can be choosen: hexagonal, rhombohedral or orthohexagonal which are represented in Figure 2.2. In most applications the hortohexagonal is preferred for simplicity. In this configuration, the $\hat{z}$ axis is identified by the optical main axis $\hat{c}$, the $\hat{y}$ axis lies on a specular reflection plane and consequently the $\hat{x}$ axis is identified. The positive direction of the $\hat{z}$ and $\hat{y}$ axes is conventionally established as the one pointing towards the surface of the crystal that is negatively charged under a compressive action along the relative axes ($\hat{z}$ and $\hat{y}$ are therefore piezoelectric directions). Moreover, the $\hat{z}$ axis is pyroelectric and the positive direction is the one towards the surface that is positively charged by cooling the crystal [24].

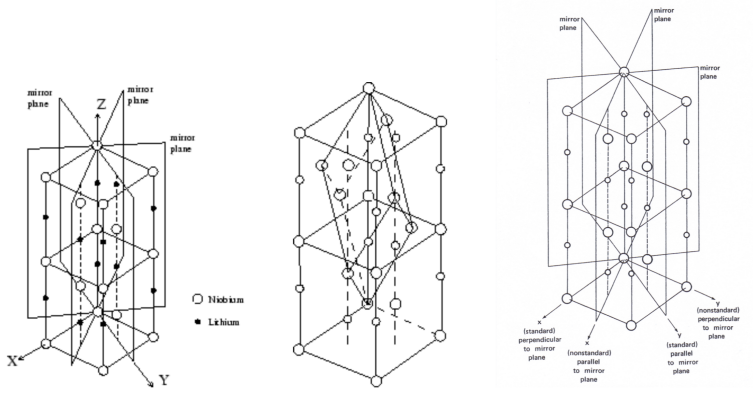

Figure 2.2: Unitary hexagonal cell with symmetry planes and cartesian reference system (left); rhombohedral cell (centre) and orthohexagonal cell (right).

Lithium niobate is a ferroelectric material, i.e. it has a spontaneous polarization that can be reversed by applying an electric field of certain magnitude. However, this property only exists below a critical temperature called Curie temperature, $T_C \simeq 1210\,°\text{C}$, beyond which the material, with the disappearance of spontaneous polarization, becomes paraelectric [25].
The crystalline structure of lithium niobate is different depending on whether the material is above or below this critical temperature. As shown in Figure 2.3, in the paraelectric phase ($T > T_C$) it consists in equidistant oxygen planes, where oxygen coordinates in triangular configurations rotated by approximately 180°; Li ions are located in the center of the oxygen triangle, while Nb ions are located at the center of an octahedron formed by two triangles. In the ferroelectric phase ($T < T_C$) the structure of the lattice is slightly different: ions move from the positions mentioned above along the optical axis $\hat{c}$ of the material giving rise to non-zero net electrical polarization within the material. In this phase the crystal exhibits a mirror symmetry about three planes that are 60° apart. The axis obtained by their intersection is the center for a three-fold rotational symmetry of the crystal. In the ferroelectric phase the interstitial sites of the octahedrons of oxygen are one third filled with Niobium atoms, one third with Lithium atoms and one third are empty, according to the sequence Nb-Li-V (where V stands for vacancy). In lithium niobate with congruent composition, moreover, some of the atoms of Nb in the material occupy the lattice site of Li remained empty because of the lower presence of Li in the material compared to the stoichiometric composition: these atoms are called Nb antisites, Nb_{Li}.

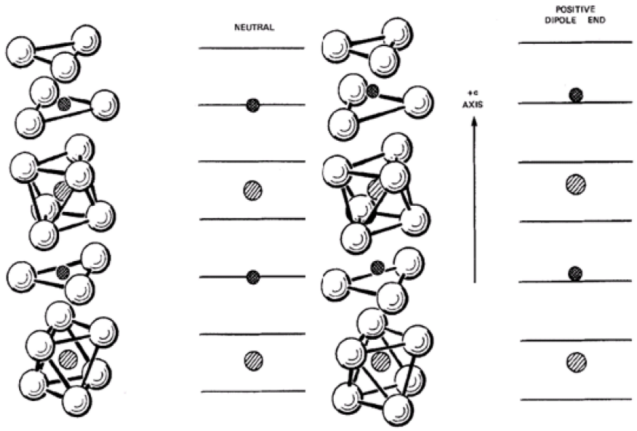

Figure 2.3: Compositional structure of lithium niobate and the sketched positions of Li and Nb atoms with respect to the oxygen planes for the paraelectric (left) and ferroelectric phase (right).

2.3 Physical and Optical Properties

Lithium niobate has many physical and optical properties. In the following the main features will be presented and the most relevant for this work, the photovoltaic effect, will be detailed in the following paragraph.

2.3.1 Piezoelectric and pyroelectric effects

As mentioned above, lithium niobate exhibits piezoelectricity since it is possible to induce polarization by applying a stress and conversely the crystals deforms elastically applying a voltage. The polarization induced along the $\hat{c}$ axis is given by $P_z^h = d_h p$ where p is the hydrostatic pressure and d_h is the hydrostatic coefficient equal to $d_h = 6.3 \cdot 10^{-12}$ C/N for $LiNbO_3$ [25].
Lithium niobate is also a pyroelectric solid which exhibits a change in the spontaneous polarization as a function of temperature. The relation between the change in temperature (ΔT) and the change in the spontaneous polarization (ΔP) is linear and can be written as $\Delta P = \hat{p}\Delta T$ where $\hat{p}$ is the pyroelectric tensor. The charge distribution due to the polarization lead to the rising of a pyroelectric field

$$\mathbf{E}_{pyro} = -\frac{1}{\varepsilon\varepsilon_0}\frac{\partial P_s}{\partial T}\Delta T \mathbf{k}_s$$

which is proportional to the change in temperature and has antiparallel orientation with respect to the spontaneous polarization direction $\mathbf{k_s}$. This field can also be generated by irradiating the crystal since the local heating leads to a change in the spontaneous polarization $\mathbf{P_s}$. Pyroelectric effect has been showed to be useful to manipulate micro and nano-droplets by elecrophoresis and trap particles via dielectrophoresis proving another possible application of lithium niobate in the field of microfluidics [9, 13].

2.3.2 Dielectric permittivity and birefringence

The optical response of an anisotropic material can be described by the dielectric permittivity tensor $\hat{\varepsilon}$, which connects the electric displacement vector $\mathbf{D}$ and the electric field $\mathbf{E}$ in the linear relation

$\mathbf{D} = \hat{\varepsilon} \cdot \mathbf{E}$. In the case of lithium niobate, with ortho-hexagonal reference system, $\hat{\varepsilon}$ is equal to

$$\hat{\varepsilon} = \begin{pmatrix} \varepsilon_{11} & 0 & 0 \\ 0 & \varepsilon_{11} & 0 \\ 0 & 0 & \varepsilon_{33} \end{pmatrix}$$

The ordinary (n_o) and extraordinary (n_e) refractive indices which refer respectively to the x, y and z axes, can therefore be written as a function of the two coefficients of dielectric permeability ε_{11} and ε_{33}:

$$n_o = \sqrt{\frac{\varepsilon_{11}}{\varepsilon_0}} \qquad n_e = \sqrt{\frac{\varepsilon_{33}}{\varepsilon_0}}$$

where ε_0 indicates the dielectric permeability in vacuum. The dispersion law $n(\lambda)$ depends not only on the wavelength but also on the temperature and concentration of lithium in the material.

2.3.3 Electro-optic effect

The electro-optic effect consists in the variation of the refractive index of the material when an electric field is applied. Changes in the refractive index can be expressed as a series of powers, truncated at the second order, with respect to the electric field $\mathbf{E}$:

$$\Delta \left(\frac{1}{n^2} \right)_{ij} = \sum_k r_{ijk} E_k + \sum_{k,l} s_{ijkl} E_k E_l$$

where the third-rank tensor r_{ijk} and the fourth-rank tensor s_{ijkl} describe the linear and the quadratic electro-optic effect, usually named *Pockels effect* and *Kerr effect* respectively. In the case of lithium niobate the variation of the refractive indices depends on the field $\mathbf{E}$: for not very intense fields, this dependence is linear. The refractive index variation depends on the incident light polarization. In the case of light polarized along the optical axis $\hat{c} \equiv \hat{z}$ and propagating either along $\hat{x}$ or $\hat{y}$ directions, a variation of the ordinary and extraordinary refractive indices occur according to the relations:

$$\Delta n_o = -\frac{1}{2} n_0^3 r_{13} E_z; \qquad \Delta n_e = -\frac{1}{2} n_e^3 r_{33} E_z \tag{2.1}$$

while in the case light is polarized either along $\hat{x}$ or $\hat{y}$ and propagates along $\hat{z}$ direction, the following relation holds:

$$\Delta n_o = -\frac{1}{2} n_0^3 r_{22} E_x; \qquad \Delta n_e = 0 \tag{2.2}$$

2.3.4 Photovoltaic effect

The bulk photovoltaic effect of lithium niobate, also known as photogalvanic effect, consists in the rising of a stationary current after the crystal is exposed to light. The observed current is proportional to the intensity of light and to the absorption coefficient of the material. This effect is due to the asymmetry of the energy bands related to ions that constitute the crystalline structure, which causes the photo-excited charge carriers to move preferably in a precise direction: this current will be described in more detail in section 2.4.

2.3.5 Photorefractive effect

The photovoltaic effect and the electro-optic effect both contribute to another peculiar phenomenon observed in lithium niobate which is called *photorefractive effect*. The photorefractive effect relies on the presence of intrinsic or extrinsic impurities with two valence states. In fact they add intermediate levels in-between the valence and conduction bands of the pure lithium niobate acting both as donors or acceptors depending on their valence state. When a non uniform light pattern irradiates the crystal, electrons in the highly illuminated areas are excited from the donor level to the conduction band. By diffusion, by photovoltaic effect or by drift they are transferred to the dark regions where they are trapped by acceptors. This lead to a non uniform charge distribution and to the rising up of an internal space-charge electric field E_{sc}.
The presence of the space-charge electric field changes the refractive index of the material by the electro-optic effect and a refractive index pattern is obtained (see Figure 2.4).

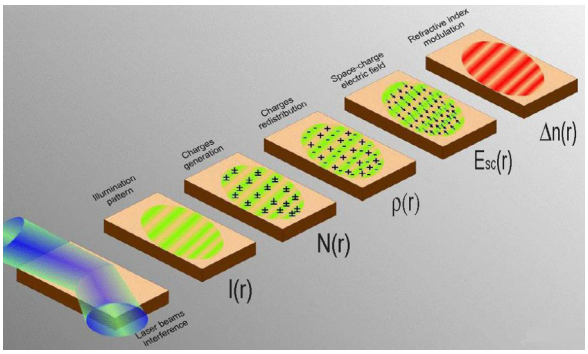

Figure 2.4: Schematic representation of the photovoltaic effect.

In lithium niobate, in addition to impurities, the niobium ions in the valence states Nb_{Li}^{5+} and Nb_{Li}^{4+} play the role of donors and acceptors respectively. The space charge fields due to niobium ions have the order of magnitude of $10^4 - 10^5$ V/m. However, it has been shown that by doping lithium niobate with transitium metals, in particular with iron, the photorefractive effect increases up to 10^6 V/m. Inside the material the iron ions appear in the valence states Fe^{2+} and Fe^{3+}: the trivalent ions act as traps for electrons, thus transforming themselves into Fe^{2+} ions, which can be photoexcited, losing an electron and returning Fe^{3+} ions.

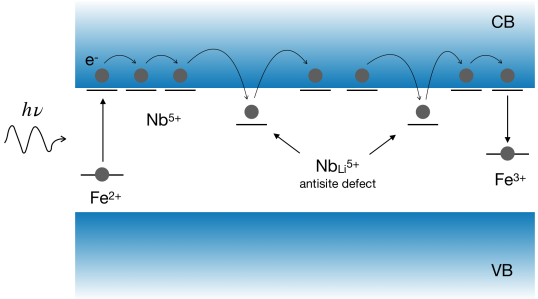

Figure 2.5: Photoexcitation scheme, promotion to the conduction band and electron trapping at Nb_{Li}^{5+} or Fe^{3+}.

2.4 Photovoltaic Effect in Fe doped Lithium Niobate

As mentioned, the photovoltaic effect conveyed by the material is a result of charge transport phenomena, which modulates the refractive index. In general, the presence of current density $\boldsymbol{j}_{tot}$ inside a lithium niobate crystal could be due to three different components: the drift current $\boldsymbol{j}_{drift}$ due to

the presence of external electric fields, the photovoltaic current $\boldsymbol{j}_{ph}$ due to the bulk photovoltaic effect and the diffusion current $\boldsymbol{j}_{diff}$. These contributions are related by the relation

$$\boldsymbol{j}_{tot} = \boldsymbol{j}_{drift} + \boldsymbol{j}_{ph} + \boldsymbol{j}_{diff} \tag{2.3}$$

In general, the total current is a function of time and space $\boldsymbol{j}(\mathbf{r}, t)$ and for the phenomenon of charge transport, the Poisson equation (2.4) and the continuity equation (2.5) hold:

$$\nabla \cdot (\hat{\varepsilon}\mathbf{E}) = \frac{\rho}{\varepsilon_0} \tag{2.4}$$

$$\nabla \cdot \boldsymbol{j} + \frac{\partial \rho}{\partial t} = 0 \tag{2.5}$$

where $\hat{\varepsilon}$ is the dielectric tensor of the material, $\rho(\mathbf{r}, t)$ the charge density, ε_0 the dielectric permittivity in vacuum and $\mathbf{E}$ the local electric field.

2.4.1 Drift current density

The Coulomb interaction between charge carriers and the external electric field determines the onset of the drift current for which the Ohm's law holds

$$\boldsymbol{j}_{drift} = \hat{\sigma}\mathbf{E} \tag{2.6}$$

$$\hat{\sigma} = q\hat{\mu}_{e,h}N_{e,h} \tag{2.7}$$

indicating with $\hat{\sigma}$ the conductivity tensor, q the elementary charge, $\hat{\mu}_{e,h}$ the mobility tensor and $N_{e,h}$ the charge carriers density (electrons in the conduction band and holes in the valence band). The total electric field $\mathbf{E}$ is the sum of three components: the space charge field $\mathbf{E}_{sc}$ arising from the internal charges redistribution, the external field $\mathbf{E}_0$ and the pyroelectric field $\mathbf{E}_{pyro}$. The latter derives from the heating of the material that can be induced by irradiation, but it's completely negligible in Fe:$LiNbO_3$ for luminous intensities lower than 10^5 W/m^2, as in the case of this study.

2.4.2 Photovoltaic current density

The photovoltaic current density $\boldsymbol{j}_{ph}$ has a linear dependence with light intensity and can be described in the following way:

$$j_{ph,i} = \beta_{ijk} e_j e_k^* \qquad i, j, k = 1, 2, 3 \tag{2.8}$$

where the complex quantity $\beta_{ijk} = \beta_{ijk}^*$ represents the photovoltaic tensor and e_j and e_k^* are the electromagnetic wave versors.
A linearly polarized wave is described by the real part of β_{ijk}, while in a circularly polarized wave also its imaginary part is involved. In lithium niobate the photovoltaic tensor has four independent non-zero components: $\beta_{333}, \beta_{311} = \beta_{322}, \beta_{222} = -\beta_{112} = -\beta_{121} = -\beta_{211}, \beta_{113} = \beta_{131}^* = \beta_{232}$.
Along the optical axis $\hat{c}$ the current density is greater, while those along $\hat{x}$ and $\hat{y}$ axis are an order of magnitude lower and they vary according to the polarization angle. This difference is due to the asymmetric energy bands relative to the ions forming the crystal structure of the material, it determines the preferential mobility of charge carriers along the $\hat{c}$ axis once they have been excited. The photovoltaic density current can be written as

$$\frac{j_{ph}}{I} = \alpha k_G = \frac{\mu \tau_{ph} E_{ph} \alpha}{h\nu} \tag{2.9}$$

where α is the absorption coefficient, k_G is a consant which describes the anisotropy of charge transport, it is called *Glass* constant and in the case of Fe:$LiNbO_3$ is equal to $2.8 \cdot 10^{-11}$ m/V , μ is the mobility of charge carriers, τ_{ph} is the time within which charge carriers contribute to the transport of photovoltaic charge, $h\nu$ is the energy of the incident photons and E_{ph} is a phenomenological field used to describe this effect acting on charge carriers.
In particular, in Fe:$LiNbO_3$ the absorption coefficient α is dependent on the donor ions concentration $[Fe^{2+}]$, hence

$$\boldsymbol{j}_{ph} = k_G \cdot \sigma \cdot [\mathrm{Fe}^{2+}] \cdot I \tag{2.10}$$

where σ is the absorption cross-section of ions Fe^{2+}.

2.4.3 Diffusion current density

The diffusion current density arises when a charge concentration gradient is established inside the material. It is generally described with the following relations:

$$\boldsymbol{j}_{diff} = -q\hat{D}\nabla N_{e,h} \qquad \hat{D} = \frac{\hat{\mu}_{e,h} k_B T}{q} \tag{2.11}$$

where $\hat{D}$ is the diffusion tensor, q the elementary charge and k_B the Boltzmann constant.

2.4.4 One-center charge transport scheme

The microscopic mechanism of charge transport in lithium niobate doped with iron is well described by the one-center model for light intensities lower than 10^6 W/m^2 and can be summarized in the following way [24]. Fe impurities are present in the $LiNbO_3$ lattice in two charge states, Fe^{2+} and Fe^{3+}, which govern the transport of free photoexcited electrons e^- according to the scheme

$$\mathrm{Fe}^{2+} + h\nu \Leftrightarrow \mathrm{Fe}^{3+} + e^- \tag{2.12}$$

where Fe^{2+} and Fe^{3+} are electron donors and traps, respectively.

The mathematical description of this model is given by the following relations:

$$\frac{\partial N_{e,h}}{\partial t} = (sI + \beta_T) N_{e,h} - \gamma_{e,h} N_{e,h} N_{\mathrm{Fe}^{3+}} - \frac{\nabla \cdot \boldsymbol{j}}{q} \tag{2.13}$$

$$\frac{\partial N_{\mathrm{Fe}^{2+}}}{\partial t} = -\frac{\partial N_{\mathrm{Fe}^{3+}}}{\partial t} = -(sI + \beta_T) N_{\mathrm{Fe}^{2+}} + \gamma_{e,h} N_{e,h} N_{\mathrm{Fe}^{3+}} \tag{2.14}$$

$$\boldsymbol{j} = q\mu_{e,h} N_{e,h} \mathbf{E} - qD\nabla N_{e,h} + sN_{\mathrm{Fe}^{2+}} k_G I \tag{2.15}$$

where $\boldsymbol{j}$ and $\mathbf{E}$ have the same direction of the optical axis $\hat{c}$ of the crystal, the density current $\boldsymbol{j} \equiv \boldsymbol{j}_{tot}$ as in equation 2.3 consequently the electric field $\mathbf{E}$ corresponds to the sum of the space charge field $\mathbf{E}_{sc}$ and the external field $\mathbf{E}_{ext}$ neglecting the pyroelectric component; $N_{e,h}$ is the charge density, s the absorption cross-section of the photon, $\gamma_{e,h}$ the recombination constant, $\mu_{e,h}$ the charge mobility, D the diffusion coefficient as in equation 2.11, β_T the thermal generation rate and $N_{\mathrm{Fe}^{2+}}$ and $N_{\mathrm{Fe}^{3+}}$ are donors and acceptors concentrations respectively.

The continuity equation and the Poisson equation can be written as

$$\nabla \cdot (\hat{\varepsilon}\varepsilon_0 \mathbf{E}_{sc}) = \rho = q(N_{e,h} + N_{\mathrm{Fe}^{2+}} - N_{\mathrm{Fe}^{2+}}(0)) \tag{2.16}$$

$$\nabla \cdot \boldsymbol{j} = -q\frac{\partial(N_{e,h} + N_{\mathrm{Fe}^{2+}})}{\partial t} \tag{2.17}$$

where $N_{\mathrm{Fe}^{2+}}(0)$ is the initial donor concentration without luminous excitation.
Since $N_{e,h} \ll N_{\mathrm{Fe}^{2+}}$ only the temporal derivative of $N_{\mathrm{Fe}^{2+}}$ can be considered applying in this way the so called *adiabatic approximation*: the concentration $N_{e,h}$ reach instantly the equilibrium value after the activation of the excitation source. During the initial transient time the space charge field $\mathbf{E}_{sc}$ has a negligible value and the adiabatic approximation can be applied since the duration of the light pulse is greater than the rising time of $N_{e,h}$. Moreover, in this case it's possible to consider $\frac{\partial N_{\mathrm{Fe}^{2+}}}{\partial t} \approx 0$, consequently:

$$N_{e,h}(\mathbf{r}, t) = \frac{(sI(\mathbf{r} + \beta_T))}{\gamma}\frac{N_{\mathrm{Fe}^{2+}}(\mathbf{r}, t)}{N_{\mathrm{Fe}^{3+}}(\mathbf{r}, t)} \tag{2.18}$$

It also follows that the conductivity (from equation 2.7) is equal to

$$\sigma = q\mu\frac{sI}{\gamma}\frac{N_{\mathrm{Fe}^{2+}}}{N_{\mathrm{Fe}^{3+}}} + q\mu\frac{\beta_T}{\gamma}\frac{N_{\mathrm{Fe}^{2+}}}{N_{\mathrm{Fe}^{3+}}} = \sigma_{ph} + \sigma_{dark} \tag{2.19}$$

This quantity results to be the sum of two different contributes: the *photoconductivity* σ_{ph} proportional to the intensity I and the *dark conductivity* σ_{dark} due to the thermal excitation of charge carriers when an external radiation source is absent. Both components are dependent on the ratio $\frac{N_{\mathrm{Fe}^{2+}}}{N_{\mathrm{Fe}^{3+}}} \equiv \frac{[\mathrm{Fe}^{2+}]}{[\mathrm{Fe}^{3+}]}$ defined as reduction degree. For light intensities greater than 1 W/cm^2, at room temperature, thermal excitation is negligible, hence $\sigma_{dark} \ll \sigma_{ph}$.

2.4.5 Writing of diffraction patterns

Photorefraction and electron redistribution discussed in the previous paragraphs generate an electric field which lead to a refractive index variation via electro-optic effect. One of the major application of this effect is the creation of diffraction gratings by means of a sinusoidal illumination. If $\mathbf{E}_{diff} \ll \mathbf{E}_{ph}$ lighting up the crystal for a time t the space charge field arises following the exponential law:

$$\mathbf{E}_{sc} = -\mathbf{E}_{ph}(1 - e^{-t/\tau}) \tag{2.20}$$

where τ is the characteristic time of the process. These quantities can be defined as follws

$$E_{ph} = \frac{k_G\gamma}{e\mu}[\mathrm{Fe}^{3+}]; \qquad \tau = \frac{\varepsilon_{33}\varepsilon_0}{\sigma_{ph}}; \qquad \sigma_{ph} = \frac{e\mu s}{\gamma}I\frac{[\mathrm{Fe}^{2+}]}{[\mathrm{Fe}^{3+}]} \tag{2.21}$$

From Equations 2.1 and 2.20 it is possible to derive the refractive index variation

$$\Delta n_e(t) = \Delta n_M(1 - e^{-t/\tau}) \tag{2.22}$$

where $\Delta n_M = -E_M n_e^3 r_{33}/2$ indicating with E_M the maximum space charge field equal to the saturation value of E_{ph}. From Equation 2.21 is clear that the characteristic time τ is inversely proportional to the reduction degree of the material, that is the ratio between the amount of donors and acceptors ($[\mathrm{Fe}^{2+}]/[\mathrm{Fe}^{3+}]$). Therefore, a way to speed up the writing process is to tune the reduction degree of the material at the expense of the space charge field directly dependent on $[\mathrm{Fe}^{3+}]$.

2.5 Optowetting on Lithium Niobate

As mentioned in the previous chapter, electrowetting allows alteration of the wetting properties of a substrate by means of free electrical charges. The wettability patterning of solid surfaces is important for different applications from integrated microfluidics to bio-chemical technologies [12]. Though electrowetting is one of the most developed technologies for liquid manipulation, some disadvantages still prevents its application for more delicate operations. Usually, the EW based experiments need complex electrode geometries to actuate and control surface wettability, not to mention that electrode creation can be in many situations a delicate and expensive operation. Moreover, conventional EW devices, designed in a certain configuration, do not allow to modify its geometry in order to use them for different purposes rather than the original one.
A possible way to overcome these obstacles is to exploit the photovoltaic effect of lithium niobate to tune the wettability of the crystal surface. In a z-cut crystal the charge separation occurs between the $+z$ and the $-z$ side of the sample, so when the material is photoexcited with light at a proper wavelength, on both sides of the crystal surface a local charge concentration appears (it is positive in the $-z$ side and negative in the opposite one). As in the case of EW, this charge accumulation will induce polarization in the molecules of a polar fluid determining a contact angle decrease. As mentioned in subsection 2.3.5, the photovoltaic effect increases significantly if the crystal is doped with iron, for this reason using iron-doped lithium niobate crystals (Fe:$LiNbO_3$) is preferable. Since the bare crystal surface is hydrophilic, with a contact angle of $\theta \approx 60°$, in order to achieve a relevant difference between lighted and dark areas a hydrophobic dielectric layer is needed, as displayed in Figure 2.6. In this work a different concept of EW based on the optical activation of a local electric field is introduced and will be called *optowetting* (OW). A prototype of OW device, sketched in Figure 2.6, has been implemented and tested with a series of systematic measurements that will be discussed in the next chapters of the thesis.

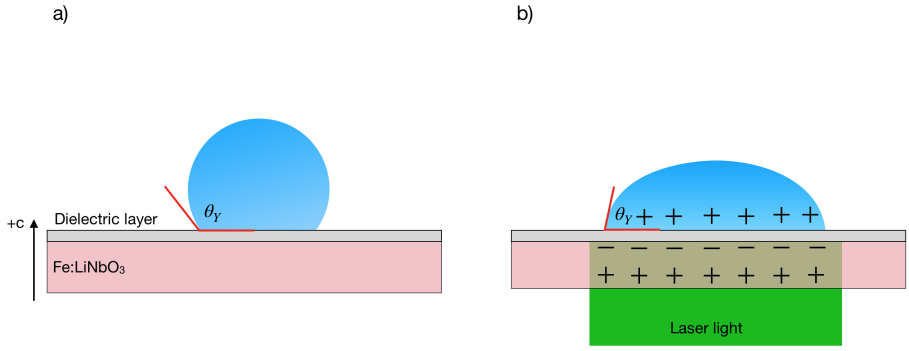

Figure 2.6: Schematic optowetting setup. a) Partially wetting liquid droplet without illumination; b) contact angle decreases when the crystal is excited with a laser.

2.5.1 Technological motivation

The novel optowetting technique presents many advantages with respect to conventional electrowetting: first, an optowetting device is realized in an electrodeless configuration since the electrodes are intrinsically embedded into the material through the local charge separation localized in the illuminated volume; last but not least, the *virtual electrodes* created by means of light are not permanent in time. In fact, once the excitation source is switched off, the electrons tends to redistribute inside the crystal riestablishing an equilibrium configuration in a characteristic time τ which depends only on the dark conductivity of the material, as reported in Equation 2.19. According to the compositional properties of the material the recombination time can range from fraction of seconds even up to days. For this reason such a device is completely reconfigurable: once a virtual electrode is vanished, a second can be written in a totally different geometry, and the write-erase procedure can be repeated

as much time as needed without damaging the crystal. Moreover, the only power source requested to activate the device is a laser light instead of a voltage generator necessary for electrowetting and there is no need of a second electrode in contact with the droplet, in other words the electronic components are extremely simplified. A direct consequence of the absence of the second electrode is that the droplet size is no limited by its presence and volumes of the order of femtoliters up to microliters can be easily controlled. As a result, the fields of application of such optowetting device not only cover those of conventional electrowetting but spread in the world of miniaturization.

Chapter 3

Sample Preparation and Characterization

This chapter is devoted to the description of the samples preparation optimized for an optowetting application. It starts with the doping of the crystal (even if not directly performed in this this work) then, with mechanical processes, the crystal surface is made optically transparent and hence the dopant composition is characterized by means of optical absorption measurements. Finally, the sample surfaces have been functionalized to be hydrophobic by testing three different chemical treatments.

3.1 Doping Lithium Niobate with Iron

The doping of a lithium niobate crystal with iron is a frequently used solution to increase the photorefractive effect up to an order of magnitude with respect to the pure crystal. This is the main reason why in this thesis work Fe:$LiNbO_3$ samples have been used. The efficacy of the photorefractive effect on the wettability change has been tested in samples having a total concentration of iron of 0.1% and different reduction degrees. These samples have been produced by $LiNbO_3$ group at the Physics department of the University of Padova and they have been doped *in bulk*, as it will be described in the following.
Many doping techniques can be used to introduce impurities, usually transition metals, in a lithium niobate crystal. For example with the Czochralski technique, dopant ions are included in the bulk material directly during the growing process, while using sputtering technique followed by thermal treatments (*in-diffused* samples) it is possible to locally dope the crystal in selected areas.
In this thesis work bulk doped crystals (i.e. prepared by Czochralski technique) were used since they have a total amount of charge donors higher than in-diffused samples, thus allowing to obtain an higher charge accumulation at the surface of the crystal.

3.1.1 Czochralski growth technique

The Czochralski technique takes its name from the polish Jan Czochralski, who first used it in 1916 studying the crystallization of metals. This method is based on the principle of liquid phase controlled solidification around a seed (or germ) of the material desired to grow, in this case $LiNbO_3$. It is performed in several phases. Initially, a pure lithium niobate germ is mounted on an alumina rod called *carrier*. The material to be crystallized is placed inside a platinum crucible and placed in a vertical tubular furnace that allows to reach the melting temperature of lithium niobate, which is about 1260°C. When the working temperature, which is higher than the melting one, is reached, the germe rod is slowly lowered and inserted into the furnace until contact with the melted material occurs. Then it is necessary to look for the dynamic equilibrium temperature for which the solidification rate is close to the melting rate. At this point the rod is raised at a constant speed of the order of mm per

hour, inducing a controlled solidification of the molten material below the germ. At the same time, the rod must also be kept rotating at a constant speed of a few rpm to counteract the natural convective movements that are created in the melt and thus obtain a flat and homogeneous interface that helps the crystal not to grow polycrystalline. As the rod rises, the temperature of the furnace is modified so that the diameter of the *boule* gradually increases from the initial diameter of the germ, called *neck*, to that of the body, thus completing the first phase that is called *shoulder*. The growth continues, keeping the diameter of the boule constant and forming what will be the body of the crystal, from which the samples will be obtained. The result is a crystal with the same crystallographic orientation as the germ used with a typical bottle shape, hence the name *boule*.

3.2 Cutting, Lapping and Polishing

The boule obtained from the growth process must be processed in order to obtain the samples to be studied. It was decided to use *z-cut* samples, i.e. obtained by cutting the main faces of the crystal perpendicular to the $\hat{z}$ axis which is also the axis of the cylindrical boule. This is because, as already mentioned, the preferential direction for the displacement of charges in the photovoltaic effect is along the optical axis $\hat{c} \equiv \hat{z}$.
The final stage of the sample preparation process consists in lapping and polishing the crystals, reducing the roughness present on the surfaces through a mechanical abrasive process. Both of these treatments are performed with a Logitech PM5 lapping machine using a rotating iron or polyurethane disc, and a device called *jig* on which the samples are mounted. The jig allows to adjust the force with which the samples are pressed on the disc and ensures that the process uniformly occurs by rotating the samples on the disc itself. The jig has a micrometer scale with a pitch of 1 μm, which indicates how much thickness has been abraded during the process. The component is supported by a mechanical arm that is kept fixed during the lapping treatment and mobile in the case of polishing, this allows to obtain a better optical quality of the final surface. The first step in this process requires the use of the iron disc together with an abrasive solution containing particles with a thickness of about 9 μm of alumina: at this stage, about 100 μm of material with an upper limit in the erosion rate of 10 μm/min is eroded. In this way, in fact, it is assured that the defects introduced during the lapping phase do not exceed three times the size of the particles that make up the solution used. The next step is to use the same disc, but with a solution of particles with a diameter of 3 μm. In this case, in order to remove all the defects created with the previous suspension (seen to be about 30 μm), at least 40 μm of surface material will be eroded. Finally, in the polishing phase the polyurethane disk and the solution with particles with diameter 0.01 μm are used. In this mode, the rate of material removal is much lower than 10 μm/min and does not create further damage to the crystal. For the polishing to be completed, at least 10 μm must be abraded to eliminate the defects created in the previous phase. The samples are then observed under a microscope to check the quality of the treated surface.

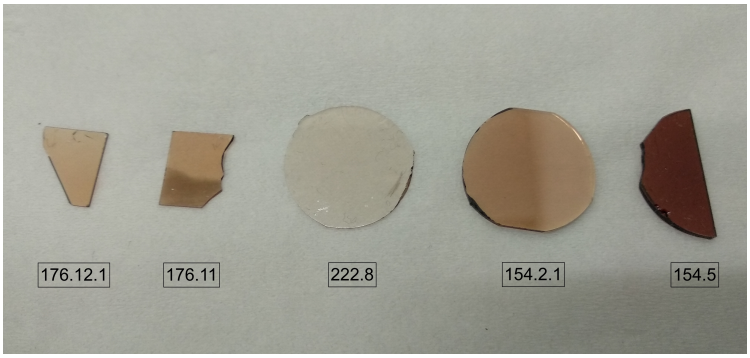

Figure 3.1: Polished Fe:$LiNbO_3$ samples used in the work.

3.3 Optical Absorption

At this point the surfaces of the samples are made sufficiently transparent so that their composition can be studied by means of optical absorption technique.
After the doping process, iron can exist inside the crystals in two possible oxidation states, 2+ and 3+. These iron ions, generally indicated with Fe^{2+} and Fe^{3+}, become photo-refractive centers acting respectively as donors and acceptors of free charges and their concentrations in the sample can be modified through reducing or oxidizing heat treatments, creating samples defined as *oxidized* (more Fe^{3+} centers) and *reduced* (more Fe^{2+} centers). The concentrations of Fe^{2+} and Fe^{3+} are crucial factors in determining the performance of the material since they govern the most important parameters involved in the photorefractive process, such as the photoconductivity, the photovoltaic current, the space-charge field and so on. Therefore it is fundamental to be able not only to change the concentration of the filled and empty traps, for instance by performing appropriate reducing thermal treatments, but also to estimate these parameters, and the optical absorption technique is a reliable method to achieved this aim.
Pure lithium niobate crystals are transparent between 0.35 μm and 4.5 μm (70-75% transparency) but the doping with iron causes the presence of absorption bands in the visible range. These bands are related to energy levels localized almost in the middle of the pure crystal band gap and they are involved in the photoinduced transition of electrons.
From the analysis of the absorption bands, previous studies demonstrated that there are four main bands with the following characteristics:

- *C band* is centered near 400 nm and involves transitions between the oxygen π-orbitals and Fe^{3+} ions;
- *D band* at about 477 nm and is due to the transitions between Fe^{2+} and Nb^{5+} leading to the creation of electrons in the conduction band formed by Nb^{5+} ions;
- two small *F bands* centered at 483 nm and 426 nm are assigned to the spin-forbidden d-d transition of Fe^{3+};
- *A band* is located at 1128 nm and involves the electronic transitions of Fe^{2+} only.

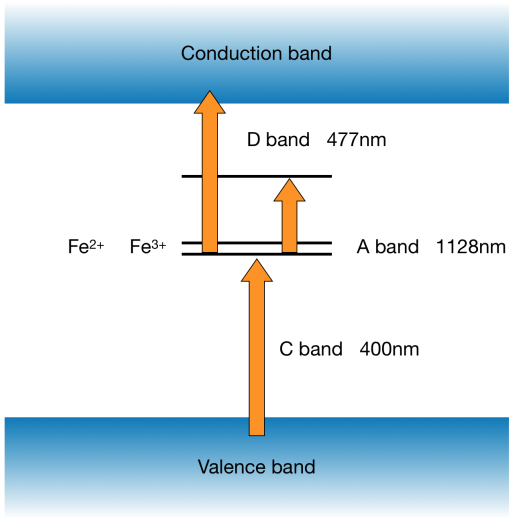

Figure 3.2: Scheme of the energetic levels of Fe:$LiNbO_3$ where the main optical transitions, A, C and D, are displayed.

Not all bands described in literature are always distinguishable because they are more or less visible depending on the concentration of the dopant and the polarization of the incident light. Experimental analyses show that *A* and *D* bands are the only ones due to electronic transitions involving only Fe^{2+}, therefore they can be used to estimate the concentration of this ion. By subtracting $[Fe^{2+}]$ from the

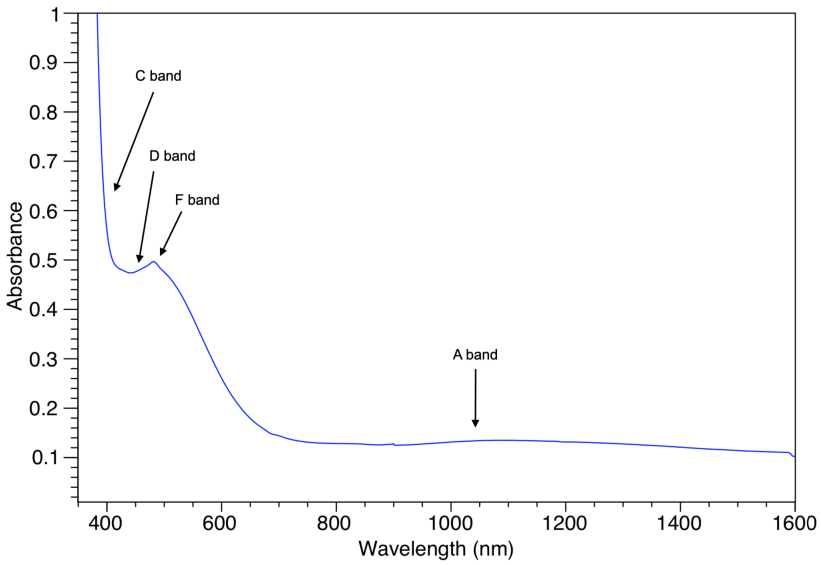

Figure 3.3: Absorption bands in the spectrum of a Fe:$LiNbO_3$ sample.

total iron concentration, the concentration of the Fe^{3+} ion is then obtained. For the aim of this work, the study of the absorption spectrum of $LiNbO_3$ samples is important mainly for the estimation of the reduction degree R of the material, which is defined as the ratio between the concentrations of donors and acceptors centers, i.e. $[Fe^{2+}]/[Fe^{3+}]$.

3.3.1 Optical spectroscopy measurements

As anticipated in the previous paragraph, the reduction degree R plays a key role in the characteristic time and intensity of the photorefractive effect in lithium niobate. This quantity was obtained by means of the optical absorption technique, using a V-670 spectrophotometer. This instrument allows to measure the percentage of absorption in a wavelength range between 190 nm and 2700 nm, thanks to the use of two different light sources, a deuterium lamp used in the ultraviolet region, and a halogen lamp used in the visible and infrared regions.
When a lithium niobate sample is illuminated by a radiation of intensity I_0, the transmitted intensity can be written as

$$I_T^{(\lambda)} = I_0 \gamma e^{-\alpha^{(\lambda)} d} \tag{3.1}$$

where γ is a coefficient which takes into account the intensity reduction due to reflection on the crystal surfaces, α is the absorption coefficient and d is the sample thickness. It has been shown experimentally that for small concentrations of dopant the Beer's law can describe the effect:

$$\alpha_{Fe^{2+}}^{(\lambda)} = [Fe^{2+}] \sigma_{Fe^{2+}}^{(\lambda)} \tag{3.2}$$

indicating with $\sigma_{Fe^{2+}}^{(\lambda)}$ the cross section of Fe^{2+} at the wavelength λ.
From the studies carried out by Berben [1] the value of the cross section at a wavelength of 532 nm can be derived:

$$\sigma_{Fe^{2+}}^{532} = (3.95 \pm 0.08) \cdot 10^{-18} \mathrm{cm}^2 \tag{3.3}$$

Once the absorption coefficient at the same wavelength is known, it is possible to obtained [Fe^{2+}]. This value is obtained by means of transmittance measurements carried out with the spectrophotometer. The transmittance is defined as the ratio between the transmitted and the incident intensity:

$$T = \frac{I_T}{I_0} \tag{3.4}$$

To obtain the value of the absorption coefficient $\alpha^{(\lambda)}_{Fe^{2+}}$, however, it is also necessary to have an estimate of the coefficient γ, as well as the transmittance. To solve this problem, the transmittance spectrum of the sample Fe:$LiNbO_3$ is normalized with respect to a pure $LiNbO_3$ with the same thickness d. Indicating with T_c the transmittance for pure niobate (*crystal*) and with T_{exp} the transmittance for iron-doped (*experimental*) niobate, it holds that:

$$\frac{T_c}{T_{exp}} = \frac{\gamma_c}{\gamma_{exp}} \frac{e^{-\alpha_c d_c}}{e^{-\alpha_{exp} d_{exp}}} = e^{(\alpha_{exp} - \alpha_c)d} \tag{3.5}$$

As a matter of fact, the refractive index of an iron-doped and a pure sample are compatible within the experimental error, and therefore the intensity of the light reflected by the surfaces of the two samples is, with good approximation, the same. In other words, the two coefficients γ_c and γ_{exp} coincide, thus being able to make the simplification in the Equation 3.5. It is worth to note that samples with the same thickness were used, so that d_c, relative to pure samples, would coincide with d_{exp}, relative to doped samples.
Introducing the absorbance $A = A_{exp}/A_c = \log(T_c/T_{exp})$, the following relation is obtained:

$$\alpha_{Fe^{2+}} = \alpha_{exp} - \alpha_c = \frac{A}{\ln(10)} d \tag{3.6}$$

Finally, from Equation 3.2 the concentration of Fe^{2+} ions is obtained.
Knowing that the nominal total concentration of iron atoms in the sample is

$$[Fe_{tot}] = (18.80 \pm 0.06) \cdot 10^{18} \text{at/cm}^3 \tag{3.7}$$

by subtraction, the concentration of Fe^{3+} ions and therefore the reduction degree R, are also computed.
In Figure 3.4 the absorption spectra related to the samples used in this thesis work are presented.

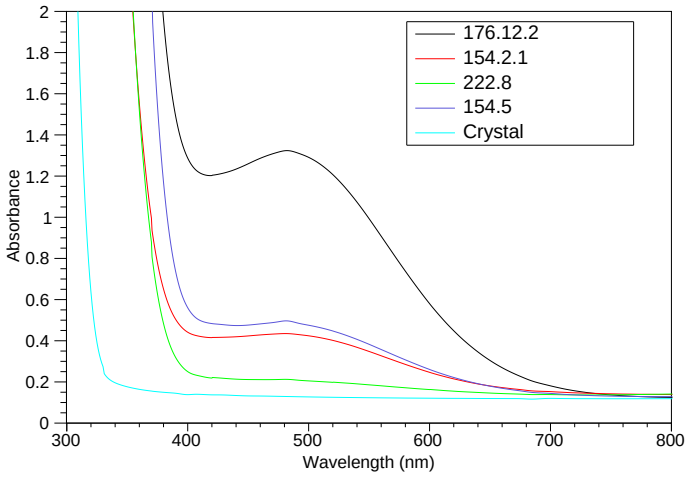

Figure 3.4: Absorbance spectra of the Fe:$LiNbO_3$ samples analysed. In the legend the sample identification numbers are indicated.

Sample	d_{exp} (mm)	Fe^{2+} (at/cm^3)	Fe^{3+} (at/cm^3)	R (%)
176.12.2	0.41 ± 0.01	$(4.7 \pm 0.1)\cdot10^{18}$	$(1.41 \pm 0.01)\cdot10^{19}$	33.8 ± 0.8
154.5	1.63 ± 0.01	$(4.0 \pm 0.1)\cdot10^{18}$	$(1.48 \pm 0.01)\cdot10^{19}$	26.7 ± 0.6
154.2.1	1.37 ± 0.01	$(1.69 \pm 0.04)\cdot10^{18}$	$(1.71 \pm 0.01)\cdot10^{19}$	9.9 ± 0.2
222.8	0.59 ± 0.03	$(1.4 \pm 0.3)\cdot10^{18}$	$(1.73 \pm 0.03)\cdot10^{19}$	9 ± 1

Table 3.1: Thickness, concentrations of Fe^{2+} and Fe^{3+} ions and reduction degree of the samples used in this work. The associated errors are derived by propagation.

As it is possible to notice, in the undoped sample and in the less reduced one (*222.8*) the absorption band centered at 477 nm is almost absent, whereas is it clearly visible in the other samples.
The concentrations of Fe^{2+} and Fe^{3+} ions as well as the reduction degree of each sample are reported in Table 3.1.

3.4 Hydrophobic Functionalizations

As introduced in section 2.5, the goal of this thesis work is to demonstrate the efficacy of an optowetting device which takes advantage of the photovoltaic effect of lithium niobate to control the motion of water droplets by modifying the wettability of the crystal surface via light illumination. The first requirement for a tunable wettability device is that the contact angle variation between the lighted and the dark regions must be at least 30° to be appreciable. The effective result of the photovoltaic effect of Fe:$LiNbO_3$ on a water droplet is a reduction of the contact angle θ due to the electrostatic attraction between water molecules and the charges on the illuminated surface of the crystal. Since the bare surface of the crystal is naturally hydrophilic with $\theta \approx 60°$, a treatment to make it hydrophobic is necessary to achieve the basic feature. Generally, silicon-based materials or depositions of fluorated compounds are used to make a surface hydrophobic. In this work three kinds of treatments have been tested: a chemical deposition of octadecyltrichlorosilane (OTS), a deposition of perfluorooctyltrichlorosilane (FTS) and a coating of polydimethylsiloxane (PDMS). In the paragraphs below, the methods used to realize the hydrophobic functionalizations of lithium niobate samples are described.

Deposition of OTS Octadecyltrichlorosilane is an amphiphilic molecule consisting of a long-chain alkyl group ($C_{18}H_{37}-$) and a polar head group ($SiCl_3-$), which forms self assembled monolayers on various oxidic substrates, as in Figure 3.5. It appears as a transparent liquid and its structural chemical formula is $CH_3(CH_2)_{17}SiCl_3$.
The procedure used to coat Fe:$LiNbO_3$ samples with OTS was a liquid phase chemical deposition: the crystal was cleaned with ethanol and distilled water; then it was immersed for 3 hours in a solution of OTS, provided by Sigma Aldrich, in toluene 5 mM and left to dry in air for one hour.

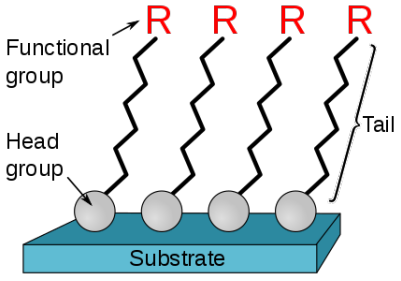

Figure 3.5: Self assembled monolayer structure.

Deposition of FTS Perfluorodecyltrichlorosilane is a colorless liquid chemical with molecular formula $C_{10}H_4Cl_3F_{17}Si$. Like OTS, FTS molecules form self-assembled monolayers and they bond onto surfaces terminated with hydroxyl (-OH) groups, such as glass, ceramics, or SiO_2 forming a regular covalent bond. It anchors on oxide surfaces with its tricholoro-silane group and attaches covalently. Due to its heavily fluorinated tail group, a FTS monolayer reduces surface energy. Generally, deposition of a FTS monolayer is achieved by a chemical deposition in vapour phase at room temperature. After cleaning the sample, it is left for one hour in a vacuum chamber together with an open beker containing 150 μL of FTS: in this way the chemical transits in the vapour phase and bonds to the surrounding surfaces, including the sample.

Deposition of PDMS Polydimethylsiloxane is the principal polymeric material used to produce elastomeric devices. It is composed of inorganic siloxane chains with organic methyl groups attached to the silicon, see Figure 3.6. This material is commercially available as a liquid pre-polymer (made by siloxane oligomers), that reticulates after mixing with a reticulant agent, in a ratio 1:10. After curing time, that could be accelerated thermally, PDMS looks like a transparent flexible elastomer.

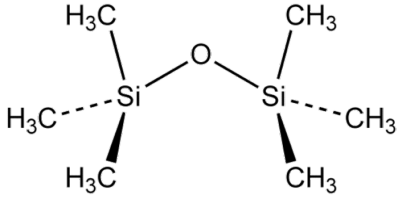

Figure 3.6: Chemical structure of PDMS

The deposition of PDMS on Fe:$LiNbO_3$ samples was done by means of spin coating technique. The instrument used in this operation is the *spin-coater* which allows to rotate the surfaces to be treated at high angular speed (up to 8000 rpm), so viscous fluids can be spread uniformly over them by means of the centrifugal force. The spin-coater can be programmed with a sequence of steps at controlled acceleration and speed and by varying the spin velocity the thickness of the layer can be tuned. The spin-coating procedure consisted of three steps, the first and second steps, each 30 s long, had spin velocity 1/10 and 1/2 of the velocity ω_{max} of the last step, that was 90 s long, respectively. A calibration of the thickness as a function of rpm was made using microscope glasses as surfaces, whose results are reported in Figure 3.7.

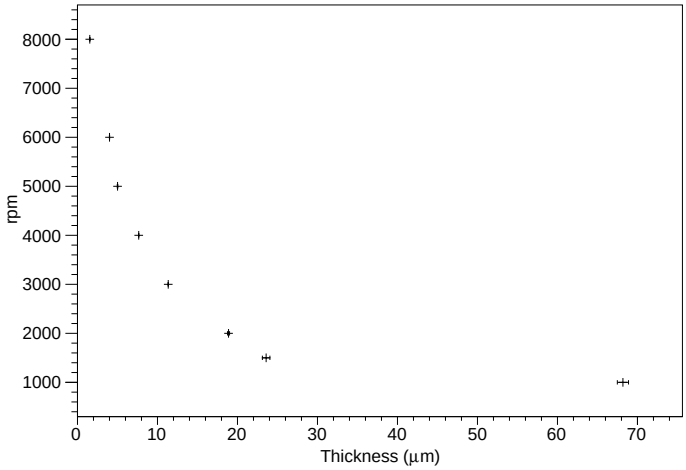

Figure 3.7: Thickness calibration of PDMS spin-coating.

During this work several samples were coated with a layer of PDMS with different thickness in order to investigate the interaction between water drops and the electric field of lithium niobate with different

dielectric thickness in between. The characterization of the crystal surfaces obtained in this way was performed by measuring the contact angle of water droplets of 1 μL volume with repeated measurements for each of the samples with the three different coatings. The description of the experimental setup and the analysis program will be treated in detail in the next chapters.

Chapter 4

Experimental Method

In this chapter the experimental setup, the measurement procedures and the methods for data analysis are described. The measurements were realized in a apparatus made up of two sections: the first is devoted to deposition of droplets with controlled volume on the upper side of the sample and to images acquisition, the second consists in an optical path aimed to properly direct the laser beam on the bottom side of the sample.

4.1 Experimental Setup

In Figure 4.1 a photo of the setup used for the contact angle measurement is displayed.

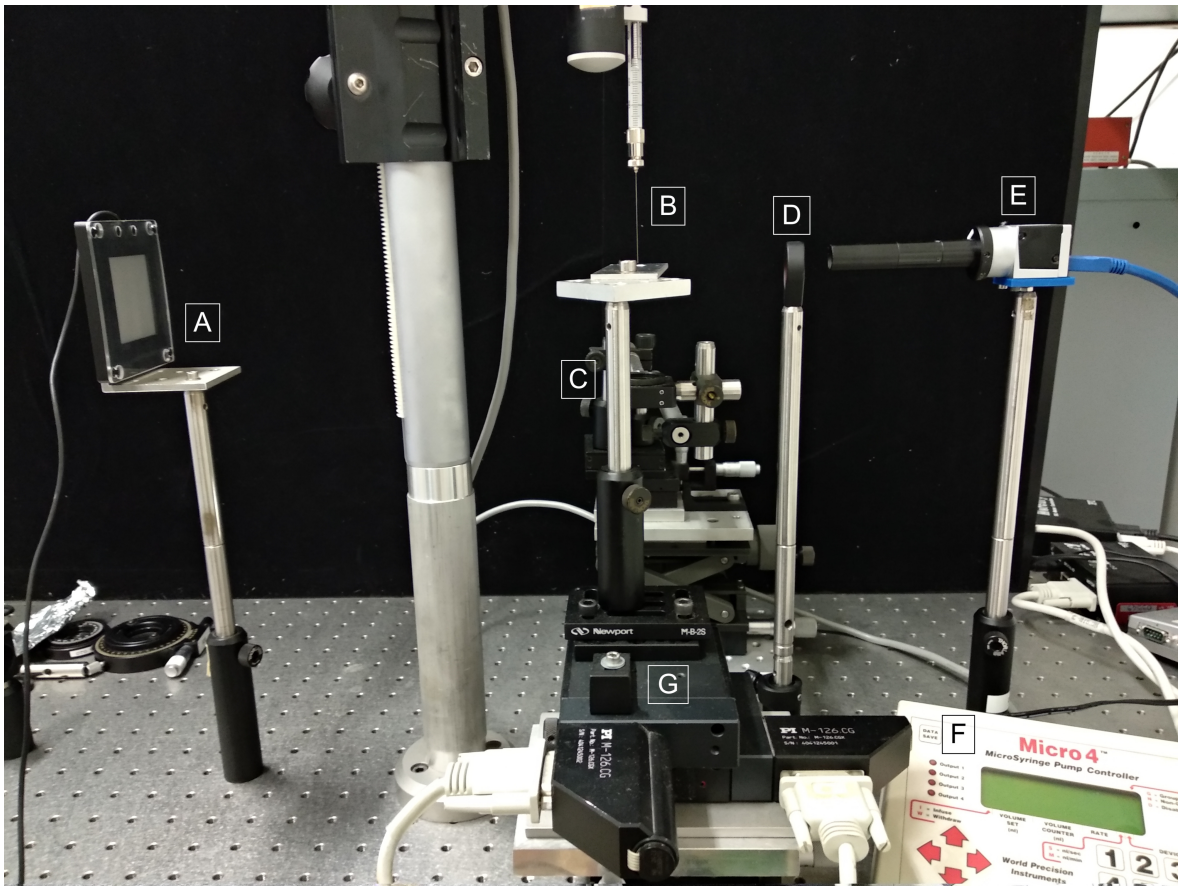

Figure 4.1: Experimental setup used for contact angle measurements. (A) white LED backlight, (B) syringe-pump with nozzle, (C) sample holder, (D) optical filter, (E) camera with 2X telecentric objective, (F) syringe-pump controller, (G) micrometric translators.

For a clearer understanding the experimental setup is sketched in Figure 4.2. The main components are:

- solid state laser at the wavelength $\lambda = 532$ nm with a beam diameter of about 2 mm and a nominal power of 100 mW;
- syringe pump equipped with a needle with an external diameter of 200 μm;
- syringe pump controller (*Word Precision Instruments, Inc*) to produce and deposit liquid drops of controlled volume on the substrate;
- CCD camera (*Basler acA800-510um*) with a telecentric objective (optical magnification 2X) to capture images and record videos of droplet profiles in order to measure the static contact angle on the sample surfaces and monitor its variation once the sample is illuminated;
- white LED light (produced by *Phlox*) to backlight the photographed object in order to obtain the contrast and brightness necessary for the images acquisition.
- holder system of the sample composed by an aluminum slab with a hole on its end with a diameter of 2 cm, smaller than the size of the samples; it allows the laser beam to illuminate the sample from the bottom. The holder system is mounted on a x-y-z micrometric translator, combined with a motorized x-y stage which allows to move the sample horizontally along a predefined path.
- optical filter ($\lambda = 532$ nm) in front of the camera to absorb the green light reflected by the water droplet when the sample is illuminated by the laser beam.

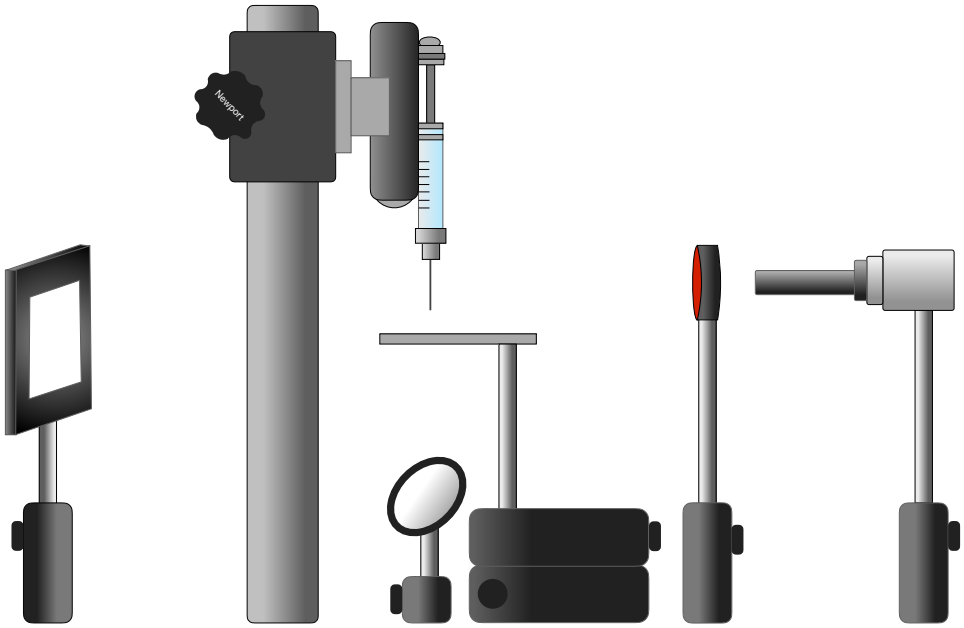

Figure 4.2: Main components of the experimental setup for the contact angle measurements: from left, the LED white light; the syringe pump holded by a adjustable support; a mirror at 45°; the sample holder with the x-y stage; the red filter and the camera equipped with the objective.

4.1.1 Optical path

The light source is a solid state laser emitting a beam at the wavelength $\lambda = 532$ nm with a power equal to 77 mW (the nominal power is 100 mW). A schematic representation of the optical path is displayed in Figure 4.3. The beam, after exiting the laser, passes through a circular variable neutral density filter ($F1$) with optical density (OD) range 0.04-4.0, used to greatly attenuate the laser intensity during the alignment phase. Then the light is reflected by two mirrors ($M1$ and $M2$) which direct it to a manual

filter wheel ($F2$) mounting a series of neutral density filters to attenuate by a desired factor the light incident on the sample. In particular, the OD 2 and OD 0.2 filters were used, which correspond to an attenuation factor of 100 and 1.6 respectively. A third mirror ($M3$) deviates the beam through an iris diaphragm (p) with a diameter of 2 mm: it was used to select the central area of the beam for an homogeneous illumination of the crystal. Finally, a fourth mirror ($M4$) positioned at 45° with respect to the incoming beam deflects the beam vertically, towards the Fe:$LiNbO_3$ sample: in this way the beam results to be perpendicular to the crystal surfaces and illuminates the sample from the bottom. A red optical filter is positioned between the sample and the camera in order to absorb the green light scattered by the droplet which could prevent a correct image acquisition.

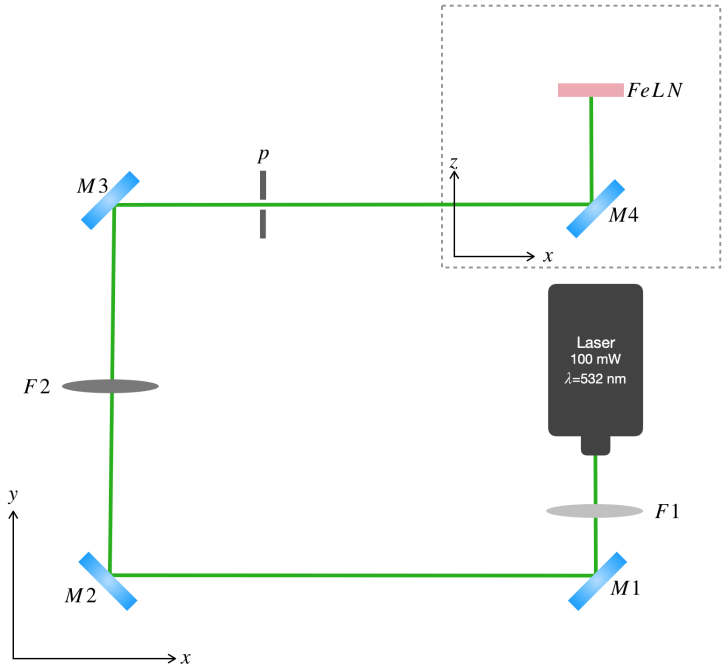

Figure 4.3: Scheme of the optical line.

Laser beam characterization The laser beam profile was characterized at the end of the optical path in correspondence of the sample holder using the laser beam profiling system provided by Coherent. Thanks to the analyser software associated to the photodiode, an image of the beam profile (reported in Figure 4.4) and some statistical analysis were obtained. The measured diameter of the beam was $d = (1.35 \pm 0.01)$ mm. The laser power was measured by means of the laser power meter *FieldMaxII-TO* provided by Coherent and its value was $P = (77 \pm 1)$ mW. Therefore, the maximum light intensity on the lithium niobate sample was $I = (54 \pm 1) \cdot 10^{-1}$ W/cm^2.

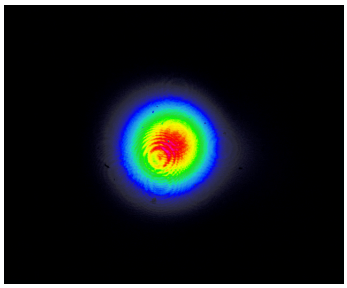

Figure 4.4: Laser profile captured with the beam viewer.

Measurement of PDMS thickness During the work, lithium niobate samples coated with layers of PDMS with different thickness were tested, as mentioned in section 3.4. The thickness of these coatings

was measured by means of a contact profile-meter: an instrument generally used to measure a surface's profile. The key component of the instrument is a rigid stylus which is moved vertically in contact with the sample and then moved laterally across the surface for a specified distance and specified contact force. A profile-meter can measure small surface variations along the vertical direction through the stylus displacement as a function of position. The profile-meter used in the work can measure small vertical features ranging in height from a few nanometres to 75 μm. The height position of the stylus generates an analogue signal which is converted into a digital signal, stored, analysed, and displayed.

4.2 Measurement Procedure

After the compositional characterization of the samples, the wettability of the surfaces treated with the three different coatings was tested. The setup sketched in Figure 4.2 combined with an ad-hoc program was used. Once the sample was positioned on the holder, a (MilliQ) water droplet with 1 μL volume was deposited on it and an image of the droplet profile was captured using the camera and the backlight. The image was processed by a *LabVIEW* program which derives the contact angles by recognizing and interpolating the drop profiles.

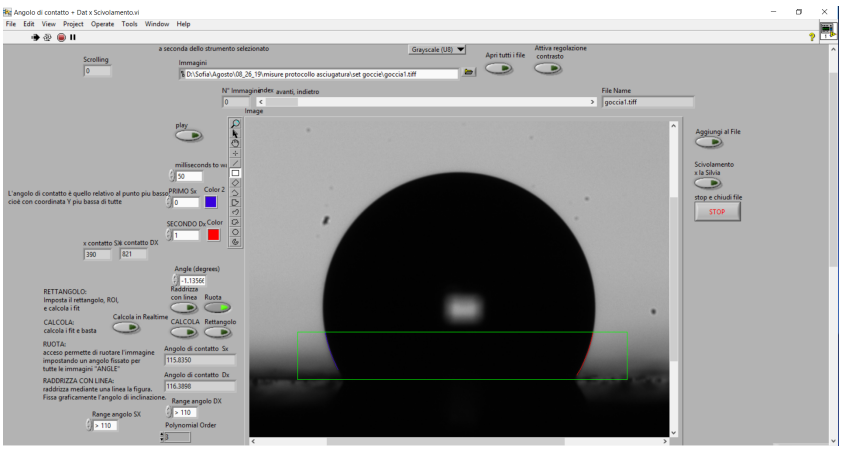

(a)

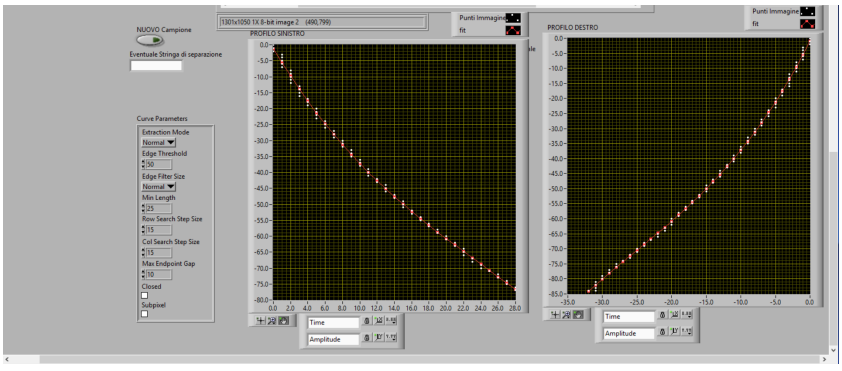

(b)

Figure 4.5: Screen of the *LabVIEW* program used to compute the contact angles from the acquired images of droplets. In the higher picture (a) the region of the photo delimited by the green rectangle is selected and in the lower part (b) the polynomial fits of the drop profiles contained in the selected area are shown.

4.2.1 Preliminary measurements

The first test that was made on the bare Fe:$LiNbO_3$ samples was aimed to check if there was an observable phenomenon on the shape of a water droplet profile due to the charge accumulation on the

crystal surface induced by light excitation.
The approach consisted simply in the deposition of a drop with 1 μL volume on the sample, switch on of the laser matching the position of the drop and observe the behaviour of the profile shape. Variations in the contact angles were observed in samples with higher reduction degrees. The same measurements were realized in samples with the hydrophobic coatings and interesting differences with respect to the bare crystals were observed, as will be discussed in the next chapter.

4.2.2 Final measurement protocol

After observing a clear and reproducible effect during the preliminary tests, a more structured and focussed method was elaborated with the purpose to identify the most suitable hydrophobic coating for the optowetting application.
The method included three main steps that involve the determination of:

- the static contact angle of the hydrophobic surface;
- the time needed to establishing the *virtual electrode* by *photoexcitation measurements*;
- the duration of the effect exerted by the *virtual electrodes* on a water droplet by *relaxation measurements*.

In the following paragraphs, each of these operations will be described.

Static contact angle measurement To determine the static contact angle (i.e. in case the contact area between liquid and solid is not changed from the outside during the measurement) of a sample, a series of drops (1 μL volume) were deposited at different points on the surface for a maximum of 20-30 drops depending on the size of the sample area. The contact angle of any drop was measured by means of the mentioned program and the final static contact angle was defined as the average of the measure of all drops. The same procedure was applied for each of the three samples with a coating of OTS, FTS and PDMS.
In Figure 4.6 some examples of drop profile acquired with the camera are presented: the four photos show the contact angle of the Fe:$LiNbO_3$ bare surface (a), the Fe:$LiNbO_3$ surface coated with FTS (b), that coated with OTS (c) and the one with a thin layer of PDMS (d).

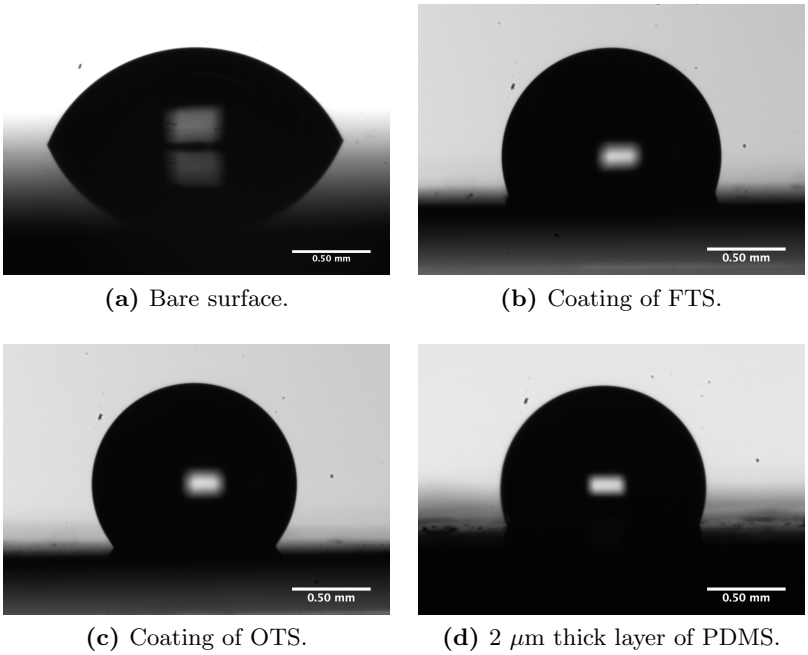

(a) Bare surface. **(b)** Coating of FTS.

(c) Coating of OTS. **(d)** 2 μm thick layer of PDMS.

Figure 4.6: Photos of 1 μL water droplets on Fe:$LiNbO_3$ samples treated with different kind of coatings.

Photoexcitation measurement The aim of these measurements was to determine the amount of time needed to illuminate the sample with the laser beam in order to achieve a reproducible change of the static contact angle. It is worth pointing out that this quantity does not correspond to the characteristic time of the photovoltaic process. In fact, as mentioned in subsection 1.3.1, in elecrowetting applications, the phenomenon of contact angle saturation occurs: beyond a certain value of the electric field the contact angle no longer decreases. So the contact angle that was be found in *saturation conditions* does not correspond to the maximum electric field created in the crystal by means of the photovoltaic effect.
The photoexcitation measurements were realized following a repetitive protocol:

1. illuminate the sample with the laser for 1 s;
2. deposit 1 μL water droplet immediately after the laser is switched off;
3. record a photo of the droplet;
4. dry the drop using paper towels;
5. re-illuminate the sample in the same point of the first step for a longer time (2 s) and repeat the procedure increasing in each measure the time of exposure to light.

Analysing each image with the dedicated program, the behaviour of the contact angle with respect to the illumination time was obtained. This relation can be described by the equation

$$\theta = \theta_A - \theta_B \cdot (1 - e^{-t/\tau}) \tag{4.1}$$

where θ_A correspond to the static contact angle without illuminating the sample and τ is a characteristic time of the phenomenon of contact angle saturation.
In subsection 2.4.5 it was explained that the characteristic time of the raising of the photovoltaic field is inversely dependent on the light intensity. To investigate if the contact angle variation shows a similar behaviour, two optical filters (with OD 2 and OD 0.2) were used to attenuate the laser beam and hence to perform the photoexcitation measurements with lower light powers, as well as to disregard the possible relation between the observation of the contact angle change and the heating of the sample.

Relaxation measurements With this kind of analysis it was possible to measure how long the virtual electrode created with light persists on the crystal surface determining a variation of its wettability. The probe used to test the effect is as always the shape of the water droplet profile.
In this case the measurement protocol consisted in the following steps:

1. illuminate the sample for 1 minute;
2. wait 1 s after the laser is switched off;
3. deposit 1 μL water droplet in the activated spot;
4. record a photo of the droplet;
5. dry the drop with paper towels;
6. re-illuminate the sample for 1 minute and repeat the steps but waiting for increasingly longer times at step 2. before placing the droplet.

This procedure was repeated for the selected samples until the waiting time was longer enough to let the photovoltaic field vanishing and recover the contact angle representative of the non-illuminated surface. The samples were lighted up each time for 1 minute because it was observed that, at the maximum available power of 77 mW, this time was sufficient to create a photovoltaic field that minimize the contact angle of the drop. In cases where an optical filter was used, the samples were excited for larger times (2 or 3 minutes).

An equivalent imaging analysis as in the previous case was conducted and the contact angle behaviour was well described by the relation:

$$\theta = \theta_A + \theta_B \cdot (1 - e^{-t/\tau}) \tag{4.2}$$

Chapter 5

Results

This chapter is devoted to the presentation and discussion of the results obtained in this work. In section 5.1 the preliminary observations are reported, then a comparison between the results obtained using samples with the three different coatings is made. Since it lead to the identification of PDMS as the best treatment, in section 5.5 a deeper study with this material is presented.

Several home-made iron doped samples differing in iron concentration, reduction degree and crystallographic cut were available for this work. Between them, four samples with the most suitable characteristics were selected to be studied. Their identifying numbers are: 222.8, 154.5, 154.2.1 and 176.12.2 and their compositional properties have been already presented in Table 3.1. In addition to these crystals, samples 176.12.1 and 176.11 were also used since they have the same dopant amount and reduction degree of sample 176.12.2 (since they have been obtained from the same boule). These three twins samples were used to investigate the effect of the thickness of the dielectric layer on the optowetting performance of lithium niobate.

5.1 Preliminary Observations

The first kind of measurement was aimed to demonstrate that the charge accumulation induced by light on Fe:$LiNbO_3$ substrates was effective in influencing the shape of a water droplet. Each of these measurements lasted about 3-4 minutes, which is a time comparable to the evaporation time of 1 μL water droplet (usually it takes about 8 minutes to completely evaporate). The evaporation mechanism of several drops was measured on a crystal surface monitoring their contact angles; by way of example, the decreasing trend of the contact angle is shown in Figure 5.1 for three drops. It can be observed that the starting contact angle is not the same for every drop: the measured value range from 55° to 70°, so the starting conditions on bare crystals are not always reproducible due to morphological characteristics of the material.

As described in subsection 4.2.1, for this check the contact angle of the droplet was monitored while the laser beam was switched on, lighting up the crystal from below. The laser beam was generally switched on 4-5 s after depositing the droplet. The right and left contact angles of the drop profile was measured as a function of time using as substrates the samples *222.8*, *154.5* and *176.12.2* without any superficial treatment; their temporal behaviour are presented in Figure 5.2.

The graphs in Figure 5.2 show very different trends. Figure 5.2a displays a constant decreasing trend over time, but a contribution related to the optowetting mechanism is not clearly visible. In fact the slope of the trending line is comparable with that of the evaporation curve. This seems to rule out both the presence of a relevant photovoltaic effect and the heating of the substrate due to light absorption (which would result in a speeding up of drop evaporation), as expected, due to the low amount of donor centers Fe^{2+}. On the contrary, by using the more reduced sample *154.5* a particular behaviour

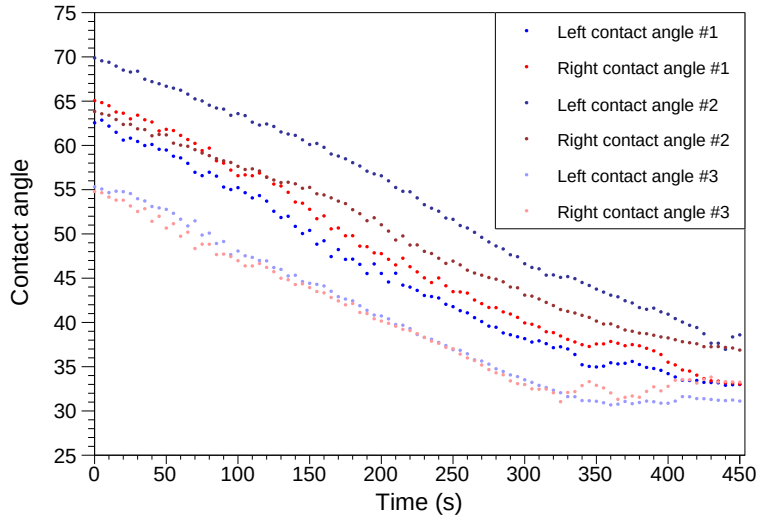

Figure 5.1: Evaporation of three water droplets with 1μL volume on a lithium niobate crystal without laser excitation.

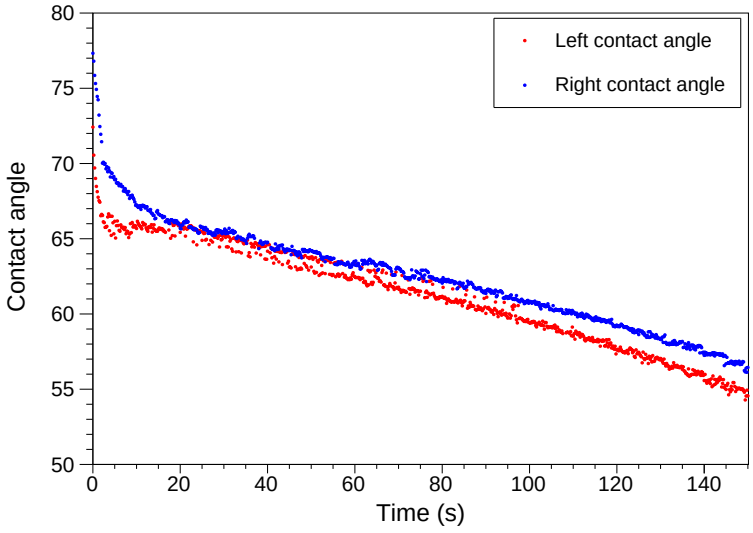

(a) Sample *222.8*, $R = 8.4\%$.

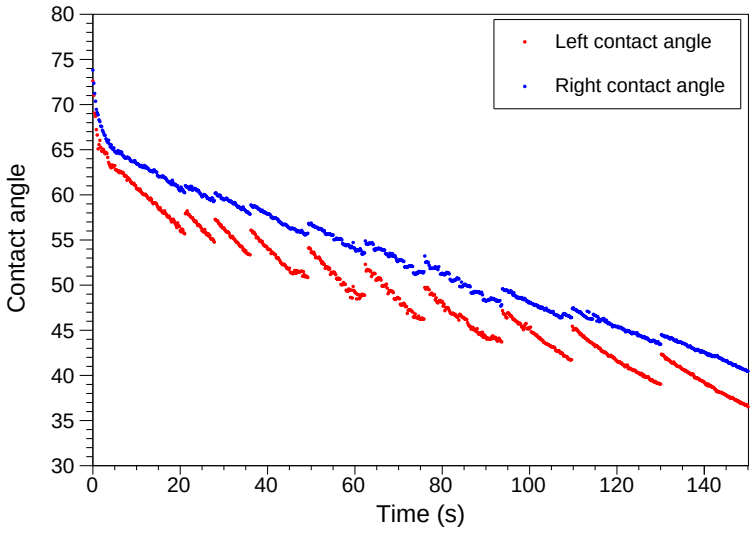

(b) Sample *154.5*, $R = 27.6\%$.

Figure 5.2: Contact angles in function of time of a water droplet on bare crystals. Blue dots indicates the right angle while red dots the left one.

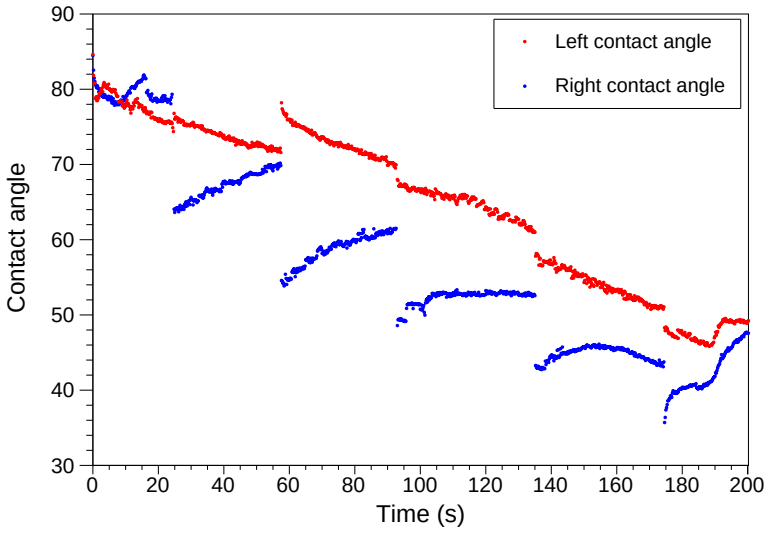

(c) Sample *176.12.2*, $R = 33.8\%$.

Figure 5.2: Contact angles in function of time of a water droplet on bare crystals. Blue dots indicates the right angle while red dots the left one.

can be recognized: there are sharp changes occurring in 0.2 s (the frame rate of image acquisition) of about 4° for the left angle and 2° for the right one. This effect is even more pronounced on sample *176.12.2* which have a reduction degree grater than the previous ones: in this case the angle variations are of 10°-15° for right contact angle and almost 5° for the left one.
These preliminary results highlight that a light-driven phenomenon occurs at the surface of reduced lithium niobate crystals and it is able to locally change the droplet shape. However, these variations are very small and not useful for actuating a droplet-controller device and the starting angles are very variable. Both these problems were solved by covering the crystal surfaces with an hydrophobic layer.

5.2 Measurements with Hydrophobic Layers

From the previous tests it was found that the sample with highest reduction degree, namely the *176.12.2*, demonstrates the most evident optowetting effect. For this reason, two identical crystals (*176.12.1* and *176.11*) were chosen to verify the efficacy of the three hydrophobic coatings on substrates having the same compositional characteristics.
The surfaces of the selected samples were treated with a liquid-phase deposition of OTS, a vapour-phase deposition of FTS and a spin-coated layer of PDMS as described in section 3.4.
The static contact angles of the hydrophobic surfaces were measured as the average between the angles of a few dozen drops for each sample. The images of a water droplet on each of the three hydrophobic layers is shown in Figure 4.6 and in Figure 5.3 the measurements of the static contact angles obtained from them are displayed; in Table 5.1 the final results are reported.

Coating	Static contact angle
OTS	117° ± 2°
FTS	108° ± 2°
PDMS	116° ± 2°

Table 5.1: Mean contact angles of the three hydrophobic surfaces.

From these contact angles measurements some differences between the three kind of hydrophobic coatings emerged. First, one can notice from Figure 5.3 that on the sample treated with OTS the measurements vary from one to another of about 10° while in the other two cases the variation is

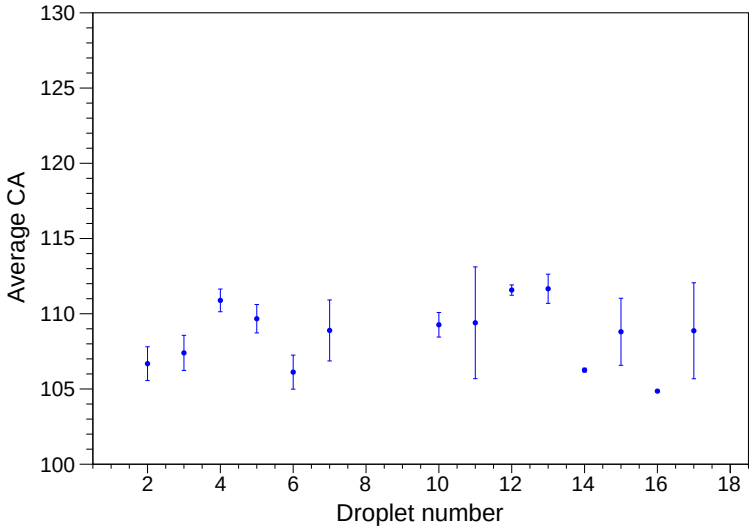

(a) Sample *176.12.1* with FTS.

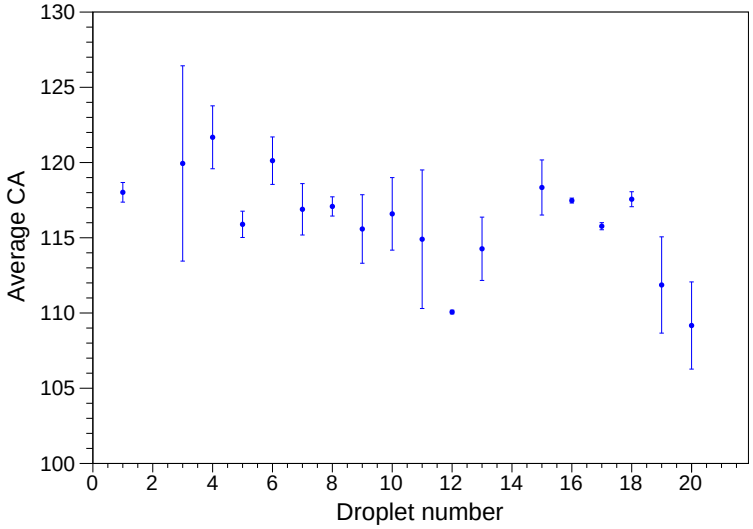

(b) Sample *176.12.2* with OTS.

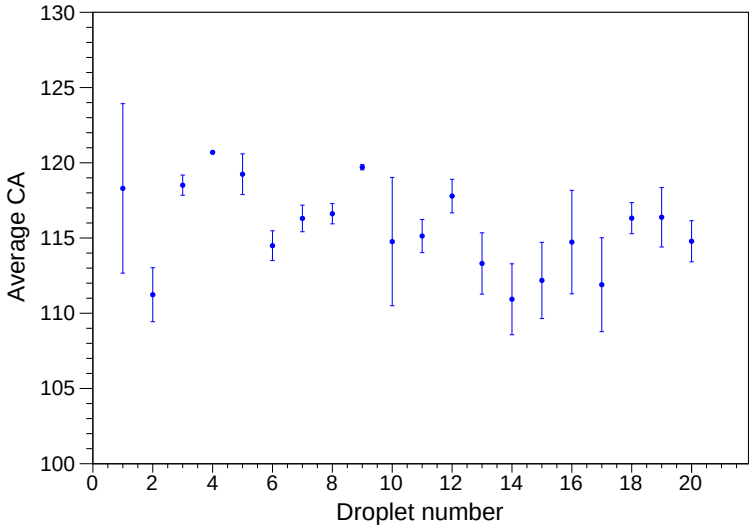

(c) Sample *176.11* with 2 μm thick layer of PDMS.

Figure 5.3: Contact angles of 1 μL water droplets on hydrophobic coatings. Blue dots represent the average between the left and right angle of the single drop profile.

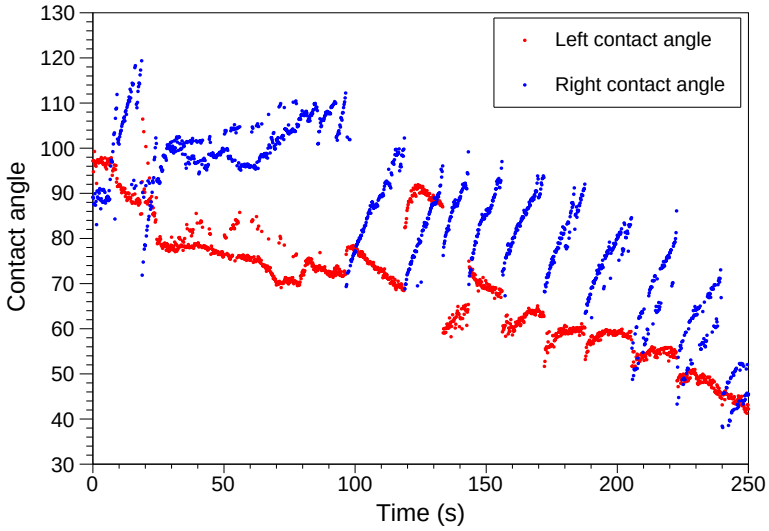

(a) Sample *176.12.2* with OTS.

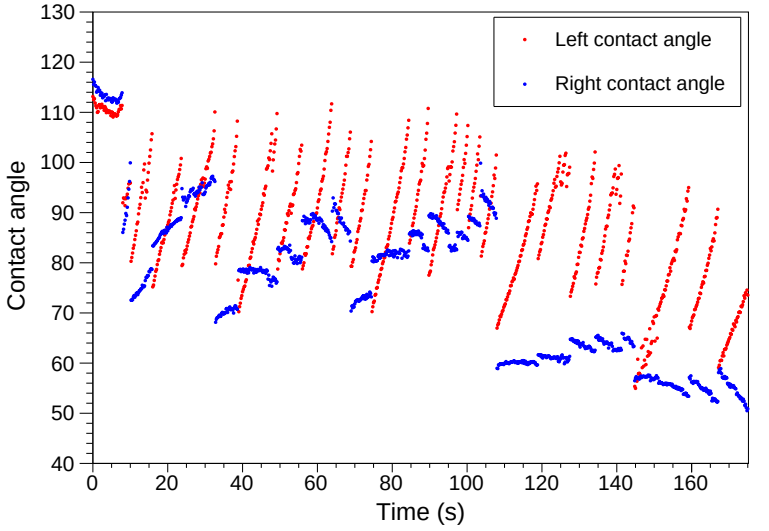

(b) Sample *176.12.1* with FTS.

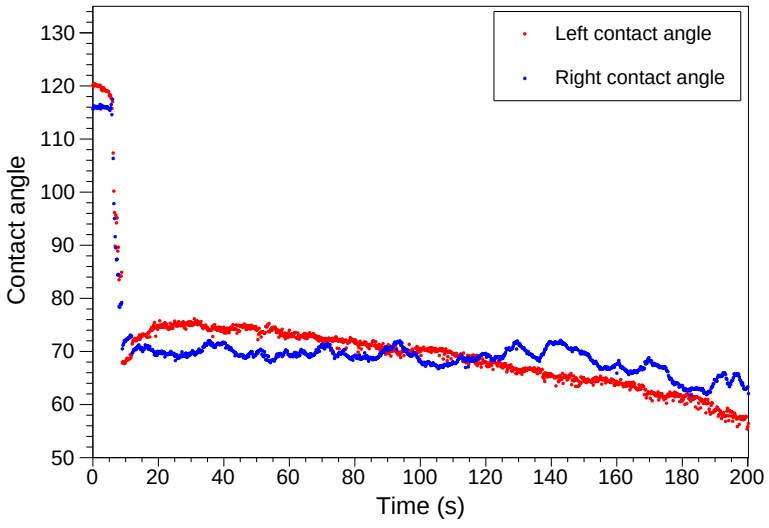

(c) Sample *176.11* with PDMS.

Figure 5.4: Contact angles as a function of time of a water droplet on crystals with hydrophobic surfaces.

slightly lower (about 7°); second, using a coating of FTS the mean contact angle is lower, as can be seen in Table 5.1.

The preparatory measurements were repeated keeping the laser switched on after depositing the drop using the coated samples described before. In Figure 5.4 the measured angles are shown. A clear amplification of the effect with respect to the bare substrate can be observed.

In Figure 5.4a and Figure 5.4b the same trend is found but with greater angle variations: the maximum jump in the case of OTS is about 30° and about 40° in the case of FTS. This *hiccup-like* trend suggest that cyclical discharge phenomena are triggered which cancel out the variation in contact angle provided by the photovoltaic effect of the crystals. It is also evident that the right and the left contact angle differ from each other: it may be due to a not perfect alignment of the laser beam with the droplet or to an asymmetry of the laser intensity profile.
Using PDMS the effect is different and it is more similar to that occurring in traditional electrowetting applications: once the sample is illuminated by the laser, the shape of the droplet changes in a stable manner for all the duration of the measurement. The droplet transits from a profile with contact angles of 118° to a different one with angles of 70°, resulting in the greatest angle variation.
The effect which determine such a different behaviour in the shape of the droplet between the samples treated with the chemical depositions and that coated with a layer of PDMS is complicated and it has not been clearly understood. More detailed studies are needed to clarify its comprehension. In figures 5.5 and 5.6 the image sequences relative to a rapid change of the contact angle are shown; they are consecutive frames of the acquisition sequence, spaced 0.2 s in time. In the first couple of pictures a difference in the left contact point is clearly visible, while in the second one the difference appears in the right angle. In the image sequence of Figure 5.7 the first picture is referred to the condition before the laser activation while the second is acquired after 40 s from the laser switching on.

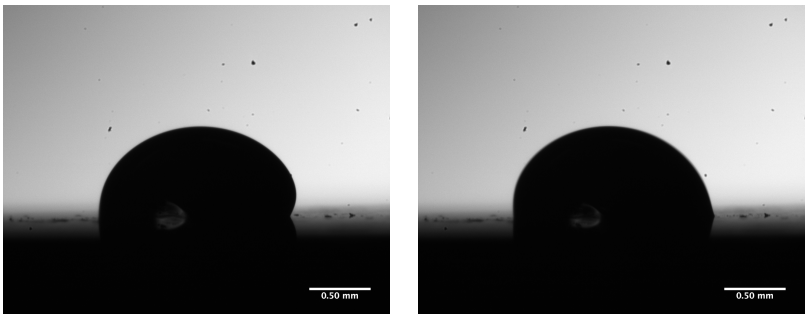

(a) **(b)**

Figure 5.5: Consecutive frames of the acquisition of water droplet on sample *176.12.2* with OTS.

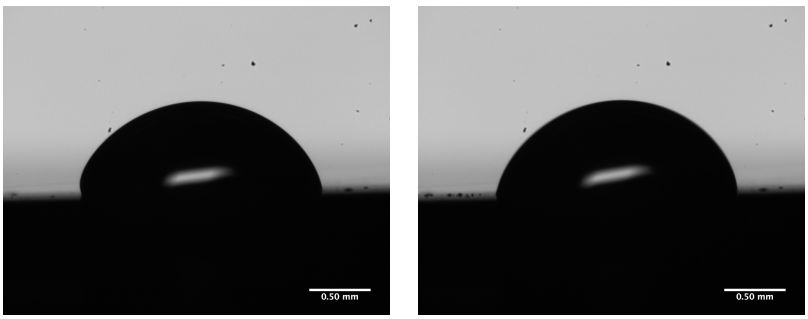

(a) **(b)**

Figure 5.6: Consecutive frames of the acquisition of water droplet on sample *176.12.1* with FTS.

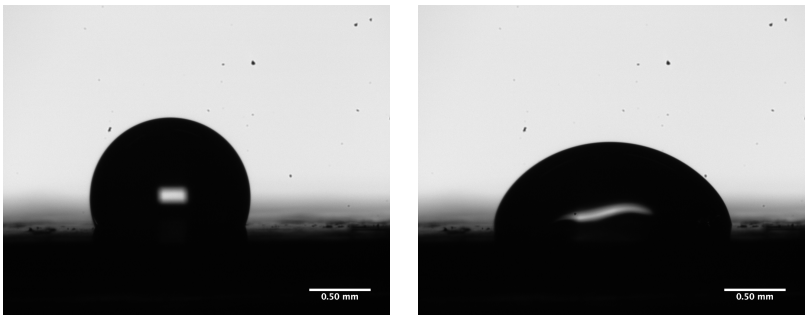

(a) **(b)**

Figure 5.7: Initial and final frames of the acquisition of water droplet on sample *176.11* with PDMS.

5.3 Photoexcitation Measurements

In this section, the results of photoexcitation measurements are presented. This study is aimed to determine the time constants typical of the optowetting phenomena on lithium niobate substrates coated with different dielectric layers. For this reason the experimental protocol was changed with respect to the previous measurements: in fact, the laser illuminates the sample only for a well-defined time before depositing the droplet, and then an image of its profile was recorded to derive the contact angle values. In contrast to the previous measurements which could be defined *dynamic* (since the laser light was kept switched on), these ones can be defined *static*. In other words, the laser was used to *activate* the substrate in order to change its wettability.
The measurement protocol actuated for this test was based on the measurement of contact angles of consecutive drops which were deposited in the same position of the crystal surface. As described in subsection 4.2.2, once a droplet was placed and the image was acquired, it was removed by drying the surface with paper towels. Then, about 30 s were waited before depositing the successive droplet, in order to let the crystal surface to completely dry. To ensure that this procedure was effective, hence that the initial conditions were the same for each drop, a series of repeated measurements were performed. In particular, the check consisted in: deposit a droplet on the sample and measure its contact angles; dry the drop and wait 30 s; place a second drop and repeat the measurement. If the starting conditions were the same, the contact angles should remain constant in all the repeated measurements. In particular, this test was performed by repeating the mentioned procedure for ten water droplets on the sample *176.11* coated with a thin layer of PDMS. In Figure 5.8 the average contact angles of these consecutive drops are displayed.

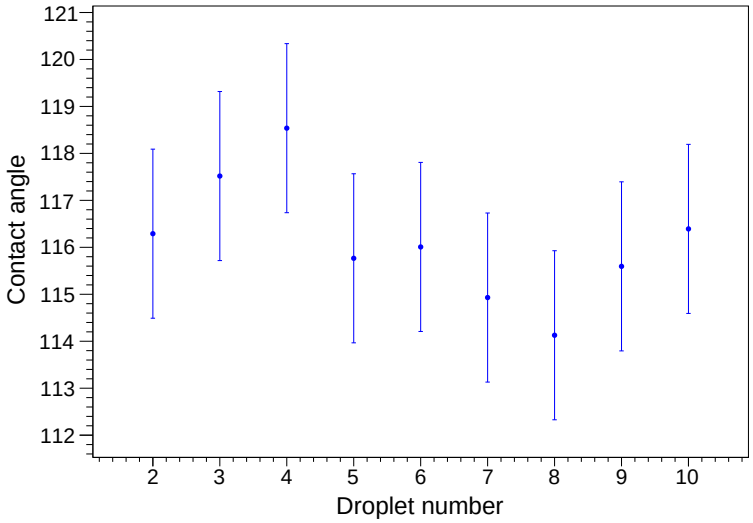

Figure 5.8: Average contact angle of successive drops in the same point of the sample to check the drying procedure.

It is evident that the presence of a previous droplet does not influence the contact angle of the successive one, since, if there was still some water on the surface, the contact angles of the successive drop would be lower than those of the previous one.
Once the drying procedure was optimized, the photoexcitation measurements were realized. In the following, the results obtained from the photoexcitation measurement are presented.
In Figure 5.9 the average between right and left contact angles of a single drop profile are plotted with respect to the illumination time (ranging between 1 and 15 s). The experimental data were fitted using the relation (Equation 4.1):

$$y = A - B \cdot (1 - e^{-Cx}) \tag{5.1}$$

and these curves are represented in the pictures as blue dotted lines. From the fitting parameters A, B and C the constant time τ and the saturation angle θ typical of the optowetting phenomenon can be derived, by means of the following formulas:

$$\tau_{phot} = \frac{1}{C} \qquad \theta_{phot} = A - B \tag{5.2}$$

The values of all the mentioned parameters are reported in Table 5.2.

	OTS	FTS	PDMS
A	109 ± 2	119 ± 2	148 ± 8
B	28 ± 2	39 ± 2	85 ± 8
C (1/s)	0.6 ± 0.1	0.25 ± 0.03	0.7 ± 0.1
τ_{phot} (s)	1.8 ± 0.2	4.0 ± 0.5	1.5 ± 0.2
θ_{phot} (°)	81 ± 3	80 ± 3	63 ± 11

Table 5.2: Fit parameters and characteristic quantities of photoexcitation measurements.

Again PDMS proved to be the best coating treatment for lithium niobate, since it allowed to reach the lowest contact angle in the steady state regime and it permitted to reach a stable configuration in a shorter time. This means that it would takes just 2 s to create a virtual electrode using a laser power of 77 mW and a PDMS thickness of 2 μm.

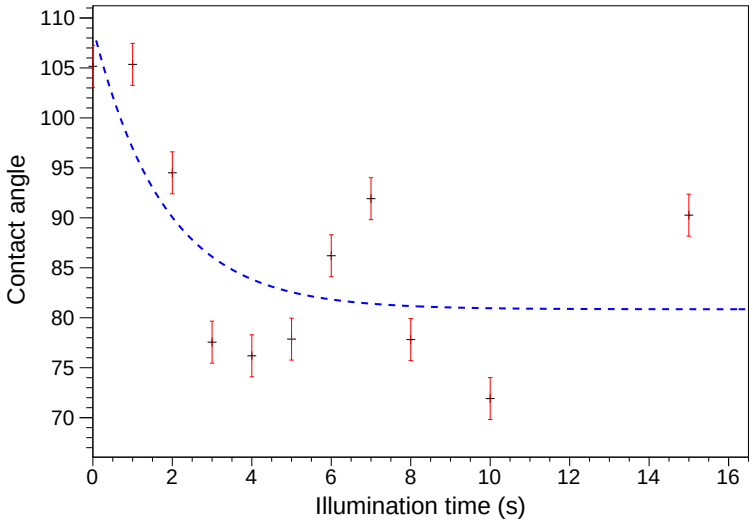

(a) Sample *176.12.2* with OTS.

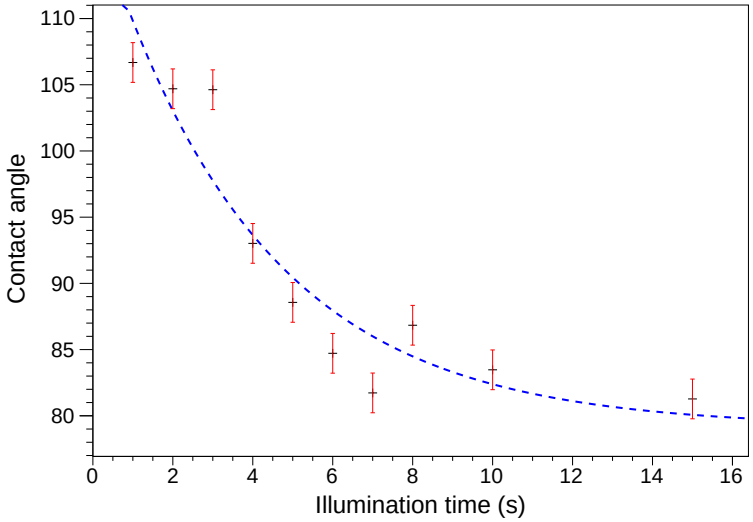

(b) Sample *176.12.1* with FTS.

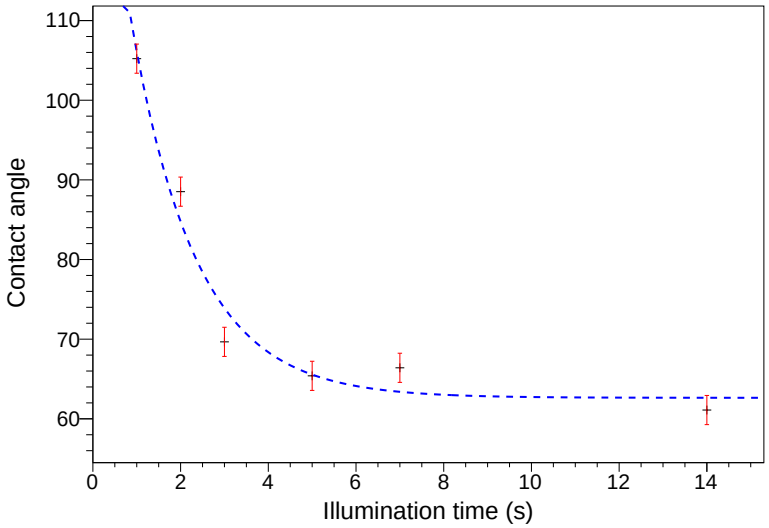

(c) Sample *176.11* with PDMS.

Figure 5.9: Photoexcitation measurements on sample with different hydrophobic coatings.

5.4 Relaxation Measurements

Relaxation measurements are the counterpart of the previous ones. The same samples were illuminated for 1 minute and the droplets were posed on them after progressively longer periods from the light switching-off. In Figure 5.10 the results are shown. The average of the left and right contact angles are plotted with respect to the waiting time after the illumination. In this case the data obtained from the three samples are very different. In cases of FTS and OTS the results are well fitted by the equation

$$y = A + B \cdot (1 - e^{-Cx}) \tag{5.3}$$

and, similarly to the photoexcitation test, the characteristic time constant and saturation angle can be found as

$$\tau_{rel} = \frac{1}{C} \qquad \theta_{rel} = A + B \tag{5.4}$$

On the contrary, the measurements obtained with PDMS do not seem to follow this trend. However, it can be noticed in Figure 5.10(c) that in this sample the restored hydrophobic angle is reached after waiting 2 hours. As a matter of fact, if the lithium niobate samples coated with FTS returns to its initial hydrophobic conditions after 15 minutes (i.e. the contact angle is close to 110°), after the same time a droplet on the PDMS-coated sample still shows a mean contact angle of only 60°. Hence, the reason why the PDMS-coated sample does not seems to behave in the same way as the other ones may be due to the fact that the restoring process is much slower and the trend should have been characterized for a longer time period to obtain a similar saturation curve.

	OTS	FTS	PDMS
A	73 ± 2	47 ± 2	-
B	18 ± 2	72.4 ± 1.9	-
C (1/s)	0.04 ± 0.02	0.0028 ± 0.0002	-
τ_{rel} (s)	24 ± 10	356 ± 23	-
θ_{rel} (°)	91 ± 3	119 ± 3	-

Table 5.3: Fit parameters and characteristic quantities of relaxation measurements.

These results confirmed that PDMS is the best solution to realize the optowetting device on lithium niobate, because both the contact angle variation and the relaxation constant time were greater than the other samples coated with OTS and FTS. For these reasons in the following sections only the PDMS coating was considered for further investigations, in particular for studying the influence of the coating thickness on the optowetting performances of the material.

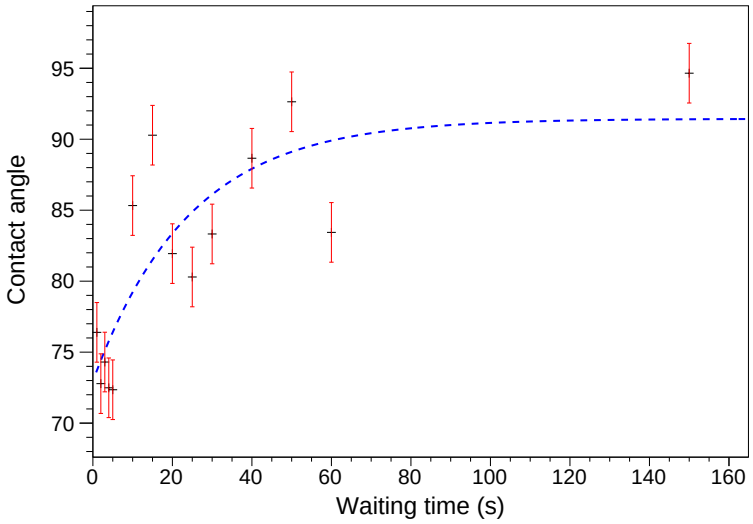

(a) Sample *176.12.2* with OTS.

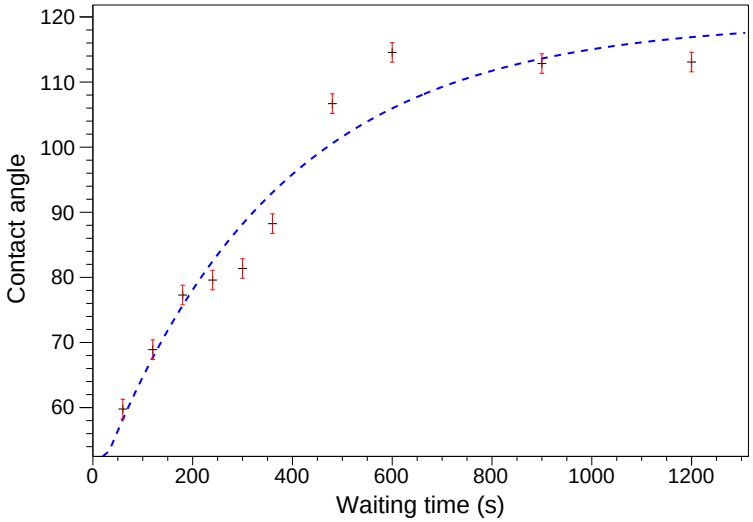

(b) Sample *176.12.1* with FTS.

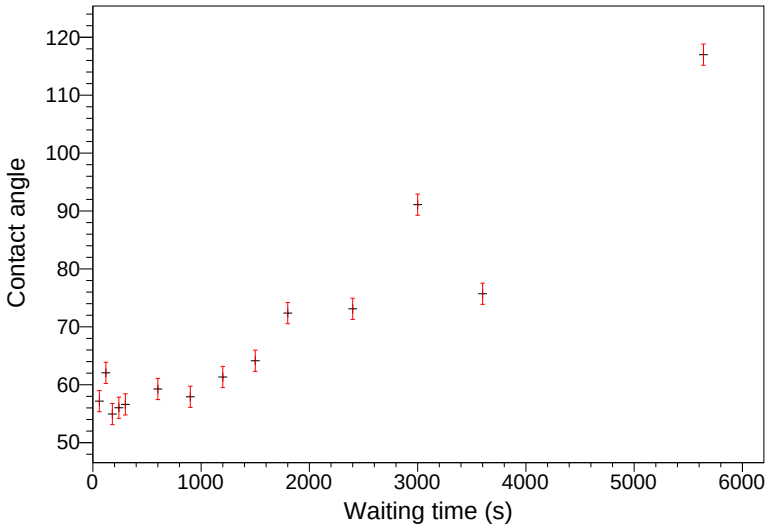

(c) Sample *176.11* with PDMS.

Figure 5.10: Relaxation measurements on z-cut LN samples with different hydrophobic coatings.

5.5 PDMS Layer Thickness Variation

By means of the spin coater, layers of PDMS with different thickness were realized on samples *176.11*, *176.12.1* and *176.12.2* which present the same compositional properties. As already mentioned, the system composed by the photorefractive material and the dielectric layer acts as a series of capacitors. By increasing the thickness of the dielectric layer, a decreasing of the characteristic time τ is expected. In fact, the total capacitance of such a system can be written as

$$C_{tot} = \left(\frac{1}{C_{LN}} + \frac{1}{C_{PDMS}} \right)^{-1} \tag{5.5}$$

where C_{LN} and C_{PDMS} are the capacitance of the lithium niobate sample and that of the dielectric, respectively. Indicating with S the sample surface, d the thickness of PDMS and ε_r the dielectric constant of the layer, the dielectric capacitance is

$$C_{PDMS} = \varepsilon_0 \varepsilon_r \frac{S}{d} \tag{5.6}$$

where for PDMS the relative permittivity is 2.3 - 2.8 [15].
If the thickness d is increased, the total capacitance will decrease and, as a result, the characteristic time $\tau = RC_{tot}$ will also decrease supposing that the crystal capacitance is kept constant.
For this reason the expected result is that, increasing the thickness of the PDMS layer, the lifetime of the virtual electrodes generated with light will be shorten.
In addiction, it is reasonable to expect that, having a thicker dielectric layer between the charged substrate and the droplet, the saturation contact angle will be greater. In fact, the electrostatic force which acts on water molecules should have a lower intensity. As a result the water droplet is attracted with lower strength on the sample surface during its deposition, and the contact angles should be greater with respect to the cases with thinner PDMS layers.

To investigate this effect, five PDMS layers with different thickness were realized and studied; their thickness, reported in Table 5.4, were measured by means of a surface profile-meter and, for the thicker ones, a micrometer screw gauge was used.

Case	Sample	PDMS thickness (μm)
1	*176.11*	1.54 ± 0.04
2	*176.11*	23.6 ± 0.5
3	*176.12.1*	68.2 ± 0.7
4	*176.12.1*	151 ± 7
5	*176.12.1*	205 ± 54

Table 5.4: Thickness of PDMS layers associated to the correspondent lithium niobate sample. For the sake of simplicity, a reference number is associated to each sample.

The results obtained using the thinnest PDMS layer are those already presented in the previous sections. In the following, the results obtained performing the same measurements described above (relaxation and photoexcitation) are introduced: in figures 5.11 to 5.14 the photoexcitation and relaxation measurements with the relative fits are displayed while in Table 5.5 the characteristic times and saturation angles are computed for each case.

From the results presented in Table 5.5 [1] it can be noted that the relaxation time τ_{rel} decreases as the thickness is increased, accordingly to the previous considerations. An unexpected result is that the saturation angle in photoexcitation measurements does not show a specific trend, but seems to be

[1] The results obtained from the measurement in case 3 are not reported since they are not in agreement with the general trend. The discrepancy could be due to defects on the PDMS layer or to errors during the coating production.

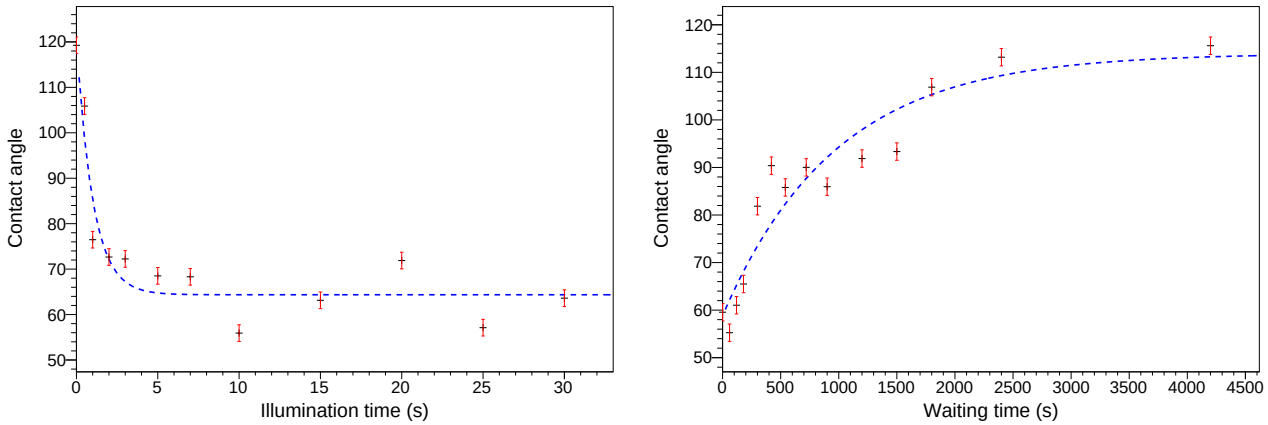

(a) Photoexcitation. **(b)** Relaxation.

Figure 5.11: Experimental results and fitting curves of case 2.

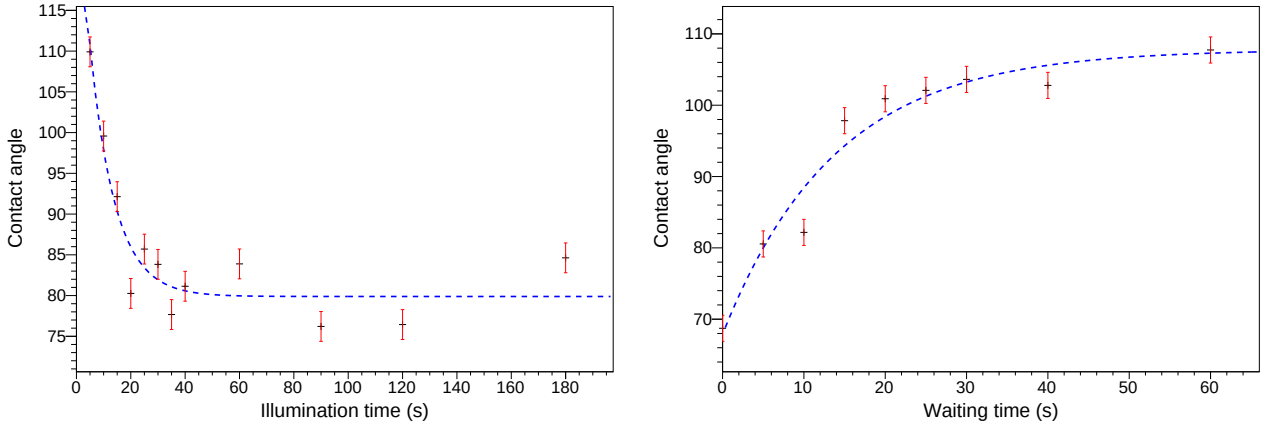

(a) Photoexcitation. **(b)** Relaxation.

Figure 5.12: Experimental results and fitting curves of case 3.

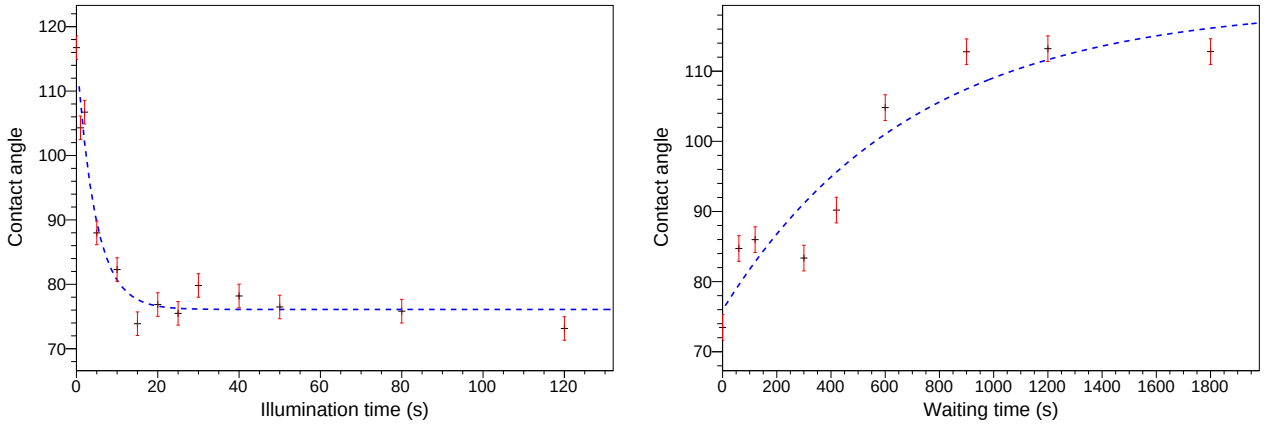

(a) Photoexcitation. **(b)** Relaxation.

Figure 5.13: Experimental results and fitting curves of case 4.

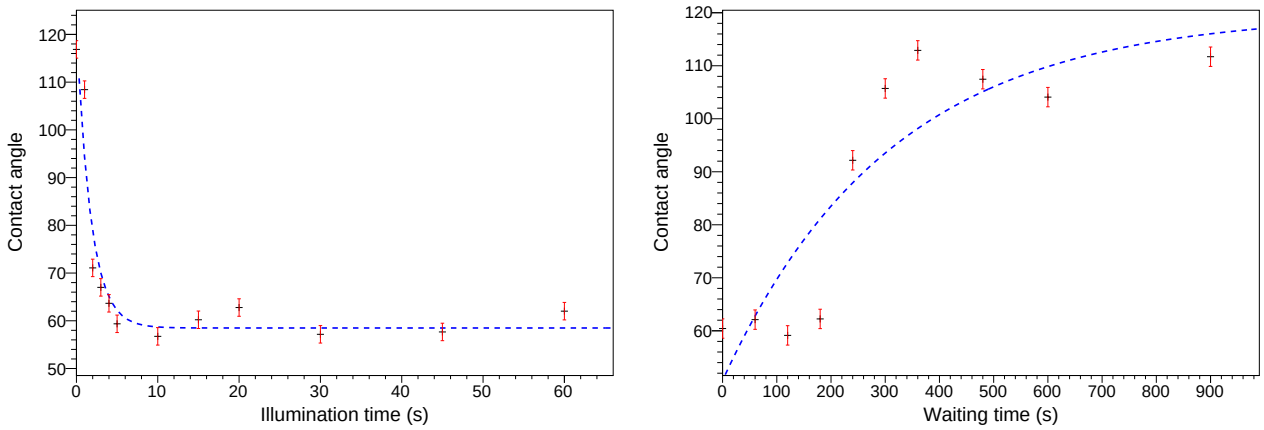

(a) Photoexcitation. **(b)** Relaxation.

Figure 5.14: Experimental results and fitting curves of case 5.

Case	τ_{phot} (s)	τ_{rel} (s)	θ_{phot} (°)	θ_{rel} (°)
1	1.5 ± 0.2	-	63 ± 11	-
2	1.0 ± 0.1	1117 ± 123	64 ± 2	114 ± 2
4	4.6 ± 0.5	972 ± 95	76 ± 2	119 ± 3
5	1.8 ± 0.1	310 ± 23	59 ± 3	120 ± 3

Table 5.5: Characteristic times and saturation angles.

unaffected by the thickness of the PDMS layer.
An additional PDMS layer with a thickness of (2.45 ± 0.02) mm was tested on sample *176.12.1*. After illuminating the sample for 1 minute, a water droplet was placed on the surface, as in the previous trials, but the contact angle variation was just of 10°, much lower than the other cases where it was at least 30°. These observations suggest that the saturation contact angle does not scale with the dielectric thickness but a threshold value may exist over which the electrostatic force is no more effective on the shape of the water droplet. This threshold could lie between 200 μm and 2 mm.

5.6 Effect of Light Intensity and Reduction Degree

The excitation light intensity is a decisive parameter for the photovoltaic effect of lithium niobate. In particular, it plays a role in the timing of photovoltaic field establishment in the crystal. The equation which describes the relation between the light intensity I and the characteristic constant time τ of the space charge field is mediated by the photoconductivity σ_{ph} which also depends on the reduction degree R of the substrate. The equations which link these parameters are the following:

$$\tau = \frac{\varepsilon_{33}\varepsilon_0}{\sigma_{ph}} \qquad \text{where} \qquad \sigma_{ph} = \frac{e\mu s}{\gamma} IR \tag{5.7}$$

The other quantities which appear in the equations are constants related to the material and to charge carriers properties (already introduced in section 2.4). These parameters are not relevant for the considerations that will be done in this section, so they can be considered as scaling constants which link the characteristic time to the photoconductivity and this one to the light intensity and the reduction degree.
From Equation 5.7 it is immediate to deduce that the time τ is inversely proportional to the light intensity and the reduction degree. In this section these dependencies are experimentally validated by relaxation and photoexcitation measurements on selected samples.

5.6.1 Variation of light intensity

The effect of different light intensities was checked with excitation measurement on sample *176.11* coated with a 2 μm thick layer of PDMS. The light intensity was modified by using neutral optical filters to attenuate the laser power. The light intensity corresponding to the maximum power was $I = 5.4$ W/cm^2; with the OD 0.2 filter the laser power was decreased by a factor 1.6 and the resulting intensity was $I' = 3.4$ W/cm^2, then using the OD 2 filter, the power was further decreased by a factor 100 and the relative intensity was $I'' = 5.4 \cdot 10^{-2}$ W/cm^2.
In Figure 5.15 the results are presented: in picture (a) the photoexcitation measurement was realized using the less absorbing filter in front of the laser, while in picture (b) the denser one was used. By comparing the time scales in the x axis of the two pictures, it is evident that there is an important correlation between the excitation intensity and the dynamics of the photovoltaic effect. In Table 5.6 the parameters resulting from the exponential fits are presented, including, for the sake of completeness, the characteristic time and saturation angle of the same measurement acquired with the maximum laser power. As expected, the characteristic time constants τ_{phot} are longer as the laser power is reduced and the saturation angles θ_{phot} are compatible with each other.

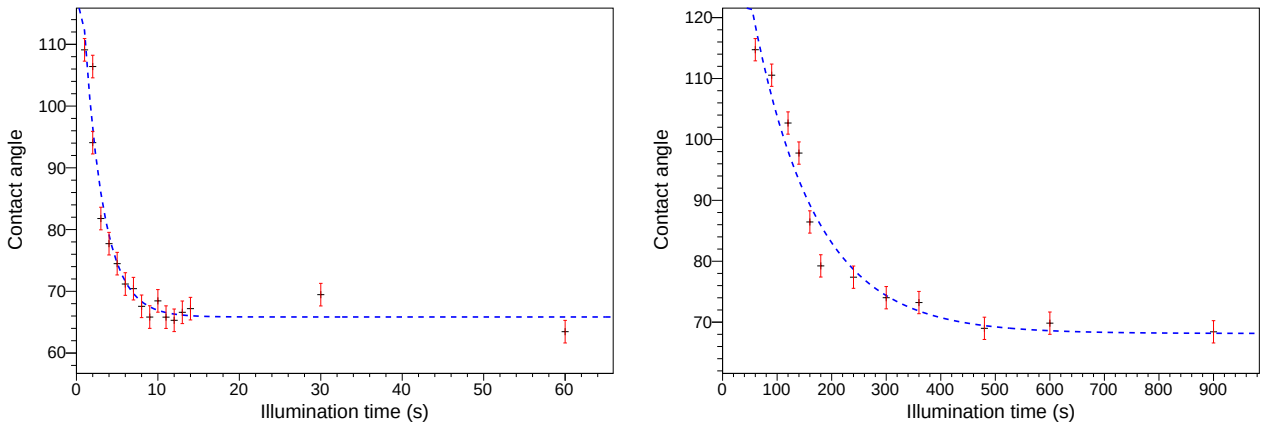

(a) Light intensity = 3.4 W/cm^2. **(b)** Light intensity = 5.4·10^{-2} W/cm^2.

Figure 5.15: Mean contact angle as a function of time during photoexcitation measurements with different light intensities. Sample *176.11* with a coating of 2 μm thick layer of PDMS.

Laser power (mW)	τ_{phot} (s)	θ_{phot} (°)
77 ± 1	1.5 ± 0.2	63 ± 11
49 ± 1	2.4 ± 0.2	66 ± 5
0.77 ± 0.01	115 ± 8	68 ± 6

Table 5.6: Comparison between photoexcitation measurements with different laser powers on sample *176.11* with a coating of 2 μm thick PDMS layer.

This test demonstrated that to create a virtual electrode on the optowetting device there is no need to use a high power laser source: in order to achieve the contact angle saturation regime it is sufficient to wait for a longer time. As a result, with a common green laser pointer, which has generally a maximum output power lower than 5 mW, the optowetting application can be implemented with low costs instruments.
Moreover, the time constants reported in Table 5.6 are of the same order of magnitude of the time constants typical of the photovoltaic phenomena. As a matter of fact, by considering a specific photoconductivity $\alpha = e\mu s/\gamma$ equal to 10^{-14} m$\Omega^{-1}W^{-1}$[24] and $\varepsilon_{33} = 28$, a photovoltaic time constant of 2 s is obtained by Equation 5.7 for the maximum laser power. This value is slightly larger than the corresponding values reported in Table 5.6, suggesting the possible presence of saturation phenomena in the optowetting mechanism on lithium niobate, so that the maximum contact angle induced by light was obtained before the maximum photovoltaic field was created at the surface of the sample.

5.6.2 Variation of reduction degree

In this section the influence of the reduction degree of iron in the Fe:$LiNbO_3$ crystals on the photovoltaic effect is studied. Photoexcitation and relaxation measurements were realized on samples *176.12.2* and *154.5* which have a reduction degree equal to 34% and 27%, respectively. In both samples an hydrophobic PDMS-coating 2 μm thick was realized in order to have the same initial conditions at the surface.
As previously mentioned, the characteristic time constant of the photovoltaic effect is inversely proportional to the reduction degree R, hence the expected result was that using as substrate the sample with higher R the characteristic time would be shorter and vice versa for the sample with lower R. The plots on Figure 5.16 and the results of the fits (reported in Table 5.7), relative to these measurements, confirmed this prediction.
In picture (a) the experimental data acquired during photoexcitation measurements are shown: the time needed to achieve the steady state regime for the contact angle in the more reduced sample is about three times lower with respect to the less reduced one. It is worth to note also that the saturation contact angles θ_{phot} differ of about 10° as well as the starting ones. This may be due to defects on the hydrophobic layer produced during the spin coating process or to its degradation after the coating deposition.
Conversely, in picture (b) the relaxation measurements for the two cases are presented. Also in this case the relation between characteristic time and reduction degree is in agreement with expectations. In addiction, the results obtained with sample *154.5* (the less reduced) are remarkable: the local photovoltaic field generated with the laser lasted for more than 15 hours, exhibiting an hydrophilic surface with a contact angle of about 70° [2].

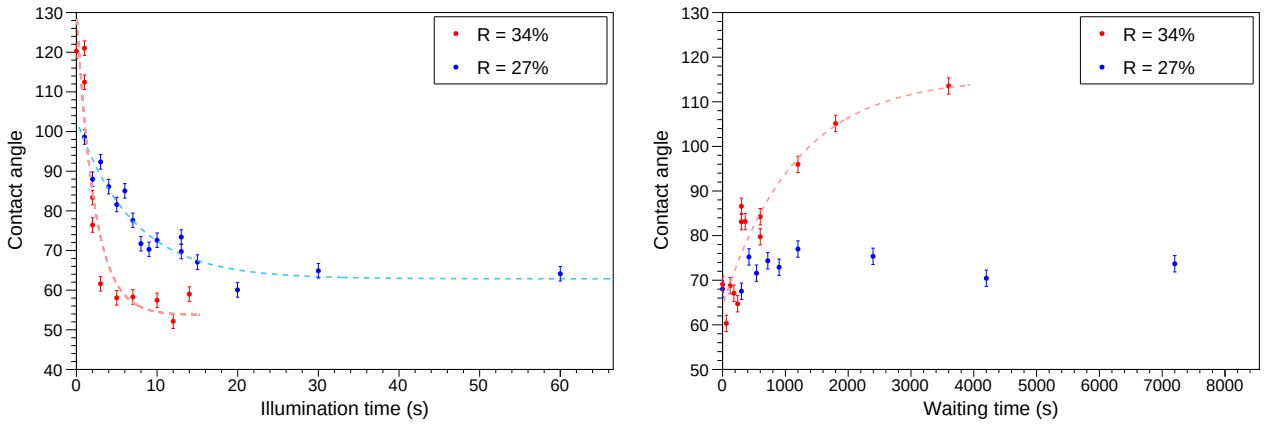

(a) Excitation measurements.

(b) Relaxation measurements.

Figure 5.16: Comparison of the dynamics of photoexcitation and relaxation effects between two samples with different reduction degrees: *154.5*, $R = 27\%$ (blue) and *176.12.2*, $R = 34\%$ (red).

R (%)	τ_{phot} (s)	τ_{rel} (s)	θ_{phot} (°)	θ_{rel} (°)
26.7 ± 0.6	7 ± 1	-	63 ± 3	-
33.8 ± 0.8	2.2 ± 0.1	1200 ± 140	54 ± 2	115 ± 3

Table 5.7: Comparison between the characteristic time and the saturation angles of the optowetting effect obtained from relaxation and photoexcitation measurements using samples with different reduction degree.

[2] In the plot represented in Figure 5.16(b) the complete dataset acquired for sample *154.5* is not displayed. The upper limit of the temporal axis has been reduced to 2h 30″ instead of 15h in order to allow the comparison between the two acquisition sets.

5.7 Validation of the Optowetting Device

As a result of the samples characterization, it was found that using as a substrate a lithium niobate crystal with reduction degree of about 34%, the local photovoltaic field created with light lasts on the surface for several hours and that the most suitable dielectric layer to perform the optowetting mechanism is a thin layer of PDMS.
To validate the feasibility of the optowetting device, a simple *proof-of-concept* test was realized, which yielded promising results. The purpose of the experiment was to demonstrate that a virtual electrode can be created on the sample surface by an optical beam and its activation affects the trajectory of a water droplet, driven by gravity. This test consisted in:

- trace an optical path with the laser across the sample;
- deposit a water droplet close to the sample edge;
- tilt the surface so that the droplet slides, driven by gravity, towards the optical path, in a direction orthogonal to the path itself.

The optical path was realized using the same setup for contact angle measurements, but with the motorized x-y stage instead of the micrometric manual translators to control the sample position. By means of the software associated to the motorized stage, the sample was translated along a straight line, keeping the laser switched on, at the lowest possible speed, so that each point of the optical path was illuminated for about 30 s. Due to the pinning exhibited by the solid PDMS surface, a small water droplet (less than 20 μL volume) is not able to slide. Using bigger drops would have not been effective to demonstrate the effect due to the limited extension of the $LiNbO_3$ surface. For this reason the surface of the sample was covered with PARAFILM tape (which consists primarily of polyolefins and paraffin waxes) over which a water droplet can slide more easily. To write a larger optical path, a Fe:$LiNbO_3$ sample different from those previously characterized was used: its identification number is *190.21* and its reduction degree is $R = (35.3 \pm 0.2)\%$, not so different from sample *176.12.2*, hence a similar optowetting performance was expected. The static contact angle of 1 μL water droplet on this surface was $\theta = 117° \pm 2°$ and it decreased of about 30° in saturation conditions when the wettability of the surface was enhanced via photovoltaic effect.
In Figure 5.17 a set of pictures represent the temporal sequence of the test. The white dotted line indicate the position of the optical path. As can be seen in the image sequence, a 10 μL volume water drop was deposited on the sample edge tilted by 70°, it slid down vertically over the sample and, when the droplet approached the optical path, it deviated to the right.
However, the drop does not ran the full length of the path, but only a segment, probably because of its high speed. In fact, in order to make the drop slide it was necessary to use a large volume and tilt the surface almost vertically: in these conditions, although the effect of the optical path was clearly observed, the drop speed was still to high to realize a practical device. Further efforts are needed to develop a slippery surface with a small hysteresis angle (i.e. the difference between the advancing and receding angles) suitable for the optowetting application, so that a droplet with a lower volume (few μL) can slides by tilting the surface by few degrees and with lower velocity.

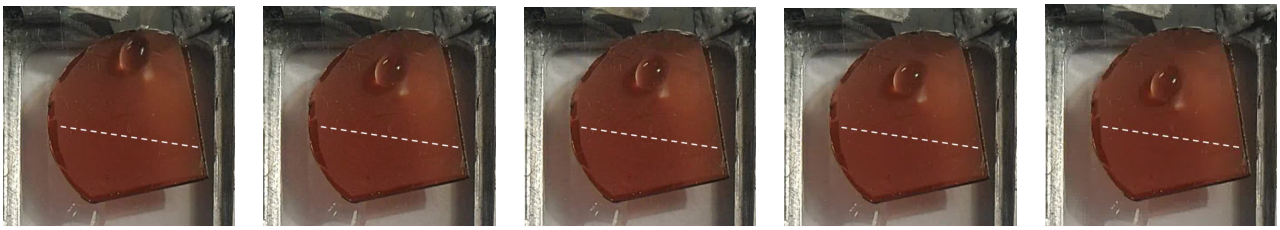

(a) 0 s. **(b)** 0.28 s. **(c)** 0.56 s. **(d)** 0.84 s. **(e)** 1.12 s.

(f) 1.4 s. **(g)** 1.54 s. **(h)** 1.68 s. **(i)** 1.82 s. **(j)** 2 s.

Figure 5.17: Temporal sequence of the test which validated the feasibility of the optowetting device. The white dotted line in each picture represents pictorially the virtual electrode created with light.

Conclusions

In this work, an optowetting device based on a lithium niobate crystal as active substrate which takes advantage of the photovoltaic effect was studied for the first time. The aim of this novel system is to manipulate aqueous droplets from nanoliters to microliters volumes in a controlled manner taking inspiration by the recently developed electrowetting devices. The major advantage of an optowetting device is that the droplet motion is controlled by means of virtual electrodes, which can be erased and re-created by the exposure to optical beams with different geometries infinite times.
A search for the best compositional properties of the lithium niobate sample was conducted to enhance this photogalvanic effect. The wettability of Fe:$LiNbO_3$ samples having different reduction degrees was evaluated through the contact angle of 1 μL volume water droplets deposited on them. The bare lithium niobate surface is naturally hydrophilic with a contact angle of about 60°. To have a larger initial contact angle and more reproducible initial conditions, three types of hydrophobic coatings were tested as dielectric layers: a liquid-phase deposition of OTS, a vapour-phase deposition of FTS and a layer of PDMS obtained by a spin-coating process. After systematic measurements it was found that a thin PDMS layer is the most suitable dielectric layer for the optowetting application. The PDMS-coated sample has a mean contact angle of 116° and the duration of the photovoltaic field is of several hours, in sharp contrast to the few minutes measured with the other coatings. The dynamics of the system was studied in detail by testing the effect of charge and discharge of the photovoltaic field on samples coated with PDMS layers with different thickness, ranging from 1.5 μm to 200 μm. Is was found that, as expected, the system behaves as a series of capacitors: the first composed by the lithium niobate crystal and the second by the dielectric layer.
Furthermore, the dependence of the characteristic time of the photovoltaic effect on light intensity and on the reduction degree was verified. As expected, illuminating the crystal with a lower light intensity required a greater exposure time to achieve a steady state contact angle. Also, using as a substrate a lithium niobate crystal with $R = 27\%$, the relaxation time of the photovoltaic field increased from 3 hours to 15 hours with respect to the more reduced one ($R = 34\%$). These observations pointed out that there exist several parameters affecting the performance of the optowetting device which include the thickness of the dielectric layer, the light intensity and the reduction degree.
Finally, a prototype of an optowetting device was realized as a *proof-of-concept* of this photogalvanic effect. A lithium niobate crystal with reduction degree equal to 35% was used as a substrate, an optical path was traced on it by a laser and a droplet with 10 μL volume was placed on its margin. When the crystal was tilted, the deposited water drop moved down driven by gravity and when it encountered the optical path it changed trajectory and followed the path.
This preliminary test proved the feasibility of the device, but further studies are needed to optimize the motion of droplets on the surface. In particular, in the final part of this thesis, an omniphobic coating of lithium niobate crystals was tested. A liquid impregnated surface formed by a piece of unlaminated membrane filter made of PTFE was attached to the crystal by capillarity and infused with a silicone oil as in [14]. Preliminary measurements proved that the optowetting effect was still evident on this new hydrophobic surface and that water droplets with only 1 μL volume could slide down the surface when it was tilted by few degrees.
The future studies on this optowetting device will proceed in this direction, focusing on a the search for a superficial hydrophobic treatment for lithium niobate crystals which provides both a small hysteresis angle for tiny water drops and is compatible with the optowetting effect, hence allowing a local change of its wettability in the regions exposed to light.

Bibliography

[1] D Berben, K Buse, S Wevering, P Herth, M Imlau, and Th Woike. Lifetime of small polarons in iron-doped lithium–niobate crystals. *Journal of applied physics*, 87(3):1034–1041, 2000.

[2] Giacomo Bettella. Integrated opto-microfluidic lab-on-a-chip in lithium niobate for droplet generation and sensing. 2016.

[3] Berge Bruno. Electrocapillarité et mouillage de films isolants par l'eau. *Comptes Rendus de L'Academie des Sciences Paris, Serie, II*, 317:157–163, 1993.

[4] Pei Yu Chiou, Hyejin Moon, Hiroshi Toshiyoshi, Chang-Jin Kim, and Ming C Wu. Light actuation of liquid by optoelectrowetting. *Sensors and actuators A: physical*, 104(3):222–228, 2003.

[5] Pierre-Gilles De Gennes, Françoise Brochard-Wyart, and David Quéré. *Capillarity and wetting phenomena: drops, bubbles, pearls, waves*. Springer Science & Business Media, 2013.

[6] Michael Esseling, Annamaria Zaltron, Nicola Argiolas, Giovanni Nava, Jörg Imbrock, Ilaria Cristiani, Cinzia Sada, and Cornelia Denz. Highly reduced iron-doped lithium niobate for optoelectronic tweezers. *Applied Physics B*, 113(2):191–197, 2013.

[7] Michael Esseling, Annamaria Zaltron, Wolfgang Horn, and Cornelia Denz. Optofluidic droplet router. *Laser & Photonics Reviews*, 9(1):98–104, 2015.

[8] Bolin Fan, Feifei Li, Lipin Chen, Lihong Shi, Wenbo Yan, Yuqing Zhang, Shaobei Li, Xuliang Wang, Xun Wang, and Hongjian Chen. Photovoltaic manipulation of water microdroplets on a hydrophobic linbo 3 substrate. *Physical Review Applied*, 7(6):064010, 2017.

[9] P Ferraro, S Coppola, S Grilli, M Paturzo, and V Vespini. Dispensing nano–pico droplets and liquid patterning by pyroelectrodynamic shooting. *Nature nanotechnology*, 5(6):429, 2010.

[10] Pietro Ferraro, Simonetta Grilli, Lisa Miccio, and Veronica Vespini. Wettability patterning of lithium niobate substrate by modulating pyroelectric effect to form microarray of sessile droplets. *Applied Physics Letters*, 92(21):213107, 2008.

[11] Nicolas Garnier, Roman O Grigoriev, and Michael F Schatz. Optical manipulation of microscale fluid flow. *Physical review letters*, 91(5):054501, 2003.

[12] Aritra Ghosh, Ranjan Ganguly, Thomas M Schutzius, and Constantine M Megaridis. Wettability patterning for high-rate, pumpless fluid transport on open, non-planar microfluidic platforms. *Lab on a Chip*, 14(9):1538–1550, 2014.

[13] Simonetta Grilli and Pietro Ferraro. Dielectrophoretic trapping of suspended particles by selective pyroelectric effect in lithium niobate crystals. *Applied Physics Letters*, 92(23):232902, 2008.

[14] Chonglei Hao, Yahua Liu, Xuemei Chen, Yuncheng He, Qiusheng Li, KY Li, and Zuankai Wang. Electrowetting on liquid-infused film (ewolf): complete reversibility and controlled droplet oscillation suppression for fast optical imaging. *Scientific reports*, 4:6846, 2014.

[15] Jude O Iroh and JE Mark. Polymer data handbook, 1999.

[16] Thomas B Jones, K-L Wang, and D-J Yao. Frequency-dependent electromechanics of aqueous liquids: electrowetting and dielectrophoresis. *Langmuir*, 20(7):2813–2818, 2004.

[17] Armelle Keiser, Ludovic Keiser, Christophe Clanet, and David Quéré. Drop friction on liquid-infused materials. *Soft Matter*, 13(39):6981–6987, 2017.

[18] Pijush K Kundu, Ira M Cohen, and HH Hu. Fluid mechanics. 3rd, 2004.

[19] Kock-Yee Law and Hong Zhao. *Surface wetting: characterization, contact angle, and fundamentals*. Springer Switzerland, 2016.

[20] Frieder Mugele and Jean-Christophe Baret. Electrowetting: from basics to applications. *Journal of physics: condensed matter*, 17(28):R705, 2005.

[21] Nam-Trung Nguyen, Sumantri Lassemono, and Franck Alexis Chollet. Optical detection for droplet size control in microfluidic droplet-based analysis systems. *Sensors and actuators B: Chemical*, 117(2):431–436, 2006.

[22] L Rebouta, MF Da Silva, JC Soares, M Hage-Ali, JP Stoquert, P Siffert, JA Sanz-Garcia, E Dieguez, and F Agulló-López. Lattice site of iron in linbo3 (fe3+) by the pixe/channelling technique. *EPL (Europhysics Letters)*, 14(6):557, 1991.

[23] Vijay Srinivasan, Vamsee K Pamula, and Richard B Fair. Droplet-based microfluidic lab-on-a-chip for glucose detection. *Analytica Chimica Acta*, 507(1):145–150, 2004.

[24] Tatyana Volk and Manfred Wöhlecke. *Lithium niobate: defects, photorefraction and ferroelectric switching*, volume 115. Springer Science & Business Media, 2008.

[25] RS Weis and TK Gaylord. Lithium niobate: summary of physical properties and crystal structure. *Applied Physics A*, 37(4):191–203, 1985.

[26] Daniel B Wolfe, Richard S Conroy, Piotr Garstecki, Brian T Mayers, Michael A Fischbach, Kateri E Paul, Mara Prentiss, and George M Whitesides. Dynamic control of liquid-core/liquid-cladding optical waveguides. *Proceedings of the National Academy of Sciences*, 101(34):12434–12438, 2004.

[27] Annamaria Zaltron. Local doping of lithium niobate by iron diffusion: a study of photorefractive properties, Doctoral thesis, Università degli studi di Padova, 2001.